J. metamorphic Geol., 2010, **28,** 227–247 doi:10.1111/j.1525-1314.2009.00864.x

Influence of tectonic overpressure on *P–T* paths of HP–UHP rocks in continental collision zones: thermomechanical modelling

Z. H. LI,[1,2] T. V. GERYA[2,3] AND J.-P. BURG[4]
[1]*School of Earth Sciences and Engineering, Nanjing University, 210093 Nanjing, China (lzhhai@gmail.com)*
[2]*Department of Earth Sciences, Geophysical Fluid Dynamics, Institute of Geophysics, ETH-Zurich, 8092 Zurich, Switzerland*
[3]*Department of Geology, Moscow State University, 119899 Moscow, Russia*
[4]*Department of Earth Sciences, Geological Institute, ETH and University of Zurich, 8092 Zurich, Switzerland*

ABSTRACT The principle of lithostatic pressure is habitually used in metamorphic geology to calculate burial/exhumation depth from pressure given by geobarometry. However, pressure deviation from lithostatic, i.e. tectonic overpressure/underpressure due to deviatoric stress and deformation, is an intrinsic property of flow and fracture in all materials, including rocks under geological conditions. In order to investigate the influences of tectonic overpressure on metamorphic *P–T* paths, 2D numerical simulations of continental subduction/collision zones were conducted with variable brittle and ductile rheologies of the crust and mantle. The experiments suggest that several regions of significant tectonic overpressure and underpressure may develop inside the slab, in the subduction channel and within the overriding plate during continental collision. The main overpressure region that may influence the *P–T* paths of HP–UHP rocks is located in the bottom corner of the wedge-like confined channel with the characteristic magnitude of pressure deviation on the order of ~0.3 GPa and 10–20% from the lithostatic values. The degree of confinement of the subduction channel is the key factor controlling this magnitude. Our models also suggest that subducted crustal rocks, which may not necessarily be exhumed, can be classified into three different groups: (i) UHP-rocks subjected to significant (≥0.3 GPa) overpressure at intermediate subduction depth (50–70 km, P = 1.5–2.5 GPa) then underpressured at depth ≥100 km ($P \geq 3$ GPa); (ii) HP-rocks subjected to ≥0.3 GPa overpressure at peak *P–T* conditions reached at 50–70 km depth in the bottom corner of the wedge-like confined subduction channel (P = 1.5–2.5 GPa); (iii) lower-pressure rocks formed at shallower depths (≤40 km depth, $P \leq 1$ GPa), which are not subjected to significant overpressure and/or underpressure.

Key words: continental collision; HP–UHP rocks; numerical modelling; *P–T* paths; tectonic overpressure.

INTRODUCTION

The regular discovery of UHP metamorphic terranes in Phanerozoic collision belts (e.g. Rosen *et al.*, 1972; Chopin, 1984; Smith, 1984; Okay *et al.*, 1989; Wang *et al.*, 1989; Sobolev & Shatsky, 1990; Xu *et al.*, 1992; Dobrzhinetskaya *et al.*, 1993, 1994, 1995) has unexpectedly and repeatedly re-invigorated the concept of subduction-exhumation of the continental crust in collision orogens. UHP rocks indicate that continental rocks may be subjected to temperatures ranging from ~700 to 950 °C and pressures from >2.8 to 5.0 GPa (UHP metamorphism; e.g. Liou *et al.*, 2004), which denotes burial of crustal rocks to depths >100 km before exhumation (e.g. Chopin, 2003). The peak depth that the HP–UHP rocks experienced is inferred from the 'lithostatic pressure' assumption, '$P = \rho g z$' (ρ is the average rock density from surface to depth z; g is the gravity acceleration). This simple relationship is a model of the lithostatic state of stress employed to translate pressure estimated from metamorphic mineral assemblages to depth.

An important concern, however, is that pressure deviation from lithostatic due to deviatoric stress and deformation (tectonic overpressure/underpressure) is an intrinsic property of flow and fracture in all materials, including rocks under geological conditions (e.g. Rutland, 1965; Brace *et al.*, 1970; Mancktelow, 1993, 1995, 2008; Petrini & Podladchikov, 2000). Therefore, one important question is whether the principle of lithostatic pressure is applicable in subduction/collision zones where crystallization and exhumation of HP–UHP rocks take place. Some authors have argued that rocks under geological conditions are too weak to support significant overpressure (e.g. Brace *et al.*, 1970; Ernst, 1971; Burov *et al.*, 2001; Renner *et al.*, 2001; Green, 2005). Yet, Stüwe & Sandiford (1994) suggested that petrologically derived *P–T* paths may not record depth changes only but stress changes. In addition, lithospheric-scale numerical models reveal regions where pressure may be hundreds of MPa or even several GPa higher or lower than lithostatic values (Mancktelow, 1993, 1995; Petrini & Podladchikov, 2000; Burg & Gerya, 2005). Mancktelow

(2008) further suggested that large magnitudes for tectonic overpressure are conceivable for strong rocks, and for highly constrained flows of relatively weak materials between strong walls, such as the configuration during extrusion or convergent channel flows. Conversely, Burov & Yamato (2008) argued that zones of anomalous pressure do not participate in the exhumation turnover, although the surrounding lithosphere of the subduction channel may be both under- and over-pressured with pressures reaching up to 1.6–2 times lithostatic; they concluded that UHP *P–T–t* data can be decoded in terms of exhumation depth using the lithostatic pressure assumption.

In this debate, three questions are formulated:

1 'Magnitude' – Is the magnitude of tectonic overpressure large enough to influence HP–UHP metamorphism in subduction zones?

2 'Spatial' – Are over-pressured rocks exhumed?

3 'Temporal' – Is overpressure at nearly peak metamorphic conditions experienced for a time sufficiently long (several million years) to be recorded and preserved by mineral equilibria?

To address these issues, we first present analytical considerations allowing approximate estimates of the magnitude of tectonic overpressure to be expected. Then the results of systematic two-dimensional (2D) thermomechanical numerical experiments of continental subduction/collision zones are described. In these experiments, a dense grid of tracing markers is used retaining information on the local *P–T* conditions. This numerical approach allows the spatial and temporal distributions of tectonic overpressure to be investigated and to test its possible influence on metamorphic *P–T* paths of HP–UHP rocks.

MAGNITUDE OF TECTONIC OVERPRESSURE: ANALYTICAL CONSIDERATIONS

Definition of pressure and overpressure

In continuum mechanics and fluid dynamics, pressure (P) is defined as the average of the diagonal components of the stress tensor (mean normal stresses):

$$P = \frac{\sigma_{xx} + \sigma_{yy} + \sigma_{zz}}{3} \tag{1}$$

with normal stresses taken as positive under compression, which is the common convention in geology and geodynamics (e.g. Turcotte & Schubert, 2002).

In the simplest tectonic models, the vertical normal stress in the z-direction is given by the weight of the overlying rock column ($\sigma_{zz} = \rho g z$), ignoring any effects of pore fluid pressure. If $\sigma_{xx} = \sigma_{yy} = \sigma_{zz} = \rho g z$, then the pressure is defined as lithostatic pressure (P_L):

$$P_L = \rho g z; \tag{2}$$

this balance between pressure and the weight of overburden is known as lithostatic state of stress (e.g. Turcotte & Schubert, 1982).

Following the definition of lithostatic pressure (P_L), the tectonic overpressure (δP) is usually defined as:

$$\delta P = P - P_L = \frac{\sigma_{xx} + \sigma_{yy} + \sigma_{zz}}{3} - \rho g z, \tag{3}$$

where P is the (dynamic) pressure, i.e. the 'total pressure'.

The full stress (tensor components σ_{ij}, where $i = x, y, z$, and $j = x, y, z$) can be subdivided into an isotropic 'pressure' (P) and an anisotropic 'deviatoric' tensor components τ_{ij}:

$$\sigma_{ij} = P\delta_{ij} + \tau_{ij}, \tag{4}$$

where δ_{ij} is the Kronecker delta, $\delta_{ij} = 1$ for $i = j$, $\delta_{ij} = 0$ for $i \neq j$.

The pressure part (P) mainly changes volumes whereas the deviatoric part (τ_{ij}) causes changes in shape, i.e. deformation.

Basic model of tectonic overpressure

The three principal stresses $\sigma_1 \geq \sigma_2 \geq \sigma_3$ are the stress components perpendicular to the three planes without shear stress, with σ_1 and σ_3 representing the maximum and minimum values of normal stress respectively. For simplicity, assuming that one of the principal stresses is vertical and the other two horizontal (so-called Anderson assumption), the tectonic pressure component (overpressure) is given by:

$$\delta P = \frac{\sigma_1 + \sigma_2 + \sigma_3}{3} - P_L \tag{5}$$

with the intermediate principal stress (σ_2) being

$$\sigma_2 = \sigma_3 + \chi(\sigma_1 - \sigma_3), \quad \text{with } 0 \leq \chi \leq 1. \tag{6}$$

1 In the horizontal compression regime, the minimum principal stress σ_3 is vertical and is equal to the lithostatic pressure ($\sigma_3 = P_L = \rho g z$). Substituting eqn 6 to eqn 5 gives,

$$\delta P = \frac{(1+\chi)(\sigma_1 - \sigma_3)}{3} \tag{7}$$

or

$$\delta P = \frac{(1+\chi)2S}{3}, \tag{8}$$

where $S = (\sigma_1 - \sigma_3)/2$ is the maximum shear stress that a rock can support. Substituting the extreme values of 0 and 1 for χ returns the limits of $2S/3$ and $4S/3$ respectively. For incompressible plane strain, $\chi = 0.5$ and $\delta P = S$.

2 In the horizontal extension regime, the maximum principal stress σ_1 is vertical and equals to the lithostatic pressure ($\sigma_1 = P_L = \rho g z$). Substituting eqn 6 to eqn 5 gives

$$\delta P = \frac{(\chi - 2)(\sigma_1 - \sigma_3)}{3} \tag{9}$$

or

$$\delta P = \frac{(\chi - 2)2S}{3}. \quad (10)$$

Substituting the extreme values of 0 and 1 for χ returns the limits of $-2S/3$ and $-4S/3$ respectively. For incompressible plane strain, $\chi = 0.5$ and $\delta P = -S$.

Considering the range in values of the three principal stresses ($\sigma_1 \geq \sigma_2 \geq \sigma_3$, so $S \geq 0$), δP is positive (overpressure) for horizontal compression and negative (underpressure) for extension. In addition, (i) the maximum magnitude of $\pm 4S/3$ for the tectonic pressure component occurs for $\sigma_1 = \sigma_2 \geq \sigma_3$ (overpressure) or $\sigma_1 \geq \sigma_2 = \sigma_3$ (underpressure); (ii) the minimum magnitude of $\pm 2S/3$ occurs for $\sigma_1 \geq \sigma_2 = \sigma_3$ (overpressure) or $\sigma_1 = \sigma_2 \geq \sigma_3$ (underpressure); and (iii) the magnitude is equal to S for incompressible plane strain conditions (Coleman & Lee, 1962; Brace *et al.*, 1970; Mancktelow, 1993, 2008).

Tectonic overpressure in the brittle regime (Mohr–Coulomb)

Petrini & Podladchikov (2000) and Mancktelow (2008) have evaluated the non-lithostatic pressure in Mohr–Coulomb brittle failure of the lithosphere. As is well established, brittle failure is dependent on the 'effective' normal stress (σ_{eff}). So the effect of fluids on the rock strength needs to be considered here, which is neglected in the former section. Fluids affect the rock strength by reducing the effective pressure and can be accounted for by introducing the pore fluid pressure ratio (λ), which is defined as the ratio between pore fluid pressure and lithostatic pressure ($\lambda = P_F/P_L$). Then the effective principal stresses in the horizontal compression regime are calculated as:

$$\begin{aligned} \sigma_{1\text{eff}} &= \sigma_1 - \lambda\sigma_3 = \sigma_1 - \lambda\rho gz \\ \sigma_{2\text{eff}} &= \sigma_2 - \lambda\sigma_3 = \sigma_2 - \lambda\rho gz \\ \sigma_{3\text{eff}} &= \sigma_3 - \lambda\sigma_3 = (1-\lambda)\rho gz. \end{aligned} \quad (11)$$

Figure 1 shows the 2D Mohr–Coulomb criterion (assuming that cohesion $C = 0$) for brittle deformation, indicating that:

$$\frac{\sigma_{1\text{eff}} + \sigma_{3\text{eff}}}{2}\sin(\varphi) = \frac{\sigma_{1\text{eff}} - \sigma_{3\text{eff}}}{2}. \quad (12)$$

Substituting eqn 11 into eqn 12 gives

$$\sigma_1 = \rho gz\frac{1 + \sin(\varphi) - 2\sin(\varphi)\lambda}{1 - \sin(\varphi)}. \quad (13)$$

Substituting eqn 13 and $\sigma_3 = \rho gz$ into eqn 7 gives

$$\delta P = \frac{2}{3}(1+\chi)\rho gz\frac{(1-\lambda)\sin(\varphi)}{1-\sin(\varphi)}, \quad 0 \leq \chi \leq 1. \quad (14)$$

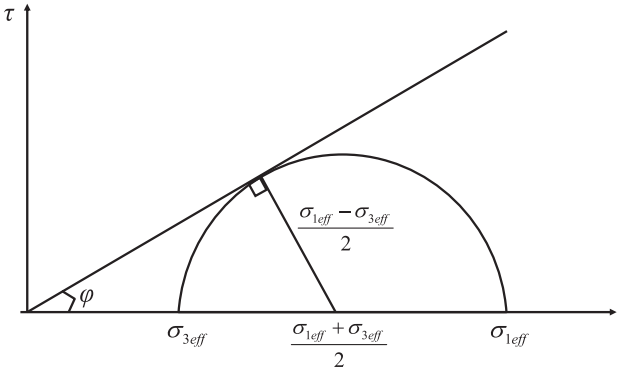

Fig. 1. Two-dimensional Mohr–Coulomb criterion (cohesion assumed to be zero).

With $\chi = 0.5$ (incompressible plane strain), $\lambda = 0$ (dry conditions) and $\varphi = 30°$ (characteristic value, e.g. Byerlee, 1978; Ranalli & Murphy, 1987), the overpressure (δP) is 'ρgz' which equals to the lithostatic value. In case of an approximately hydrostatic pore fluid pressure ($\lambda = 0.4$), the overpressure (δP) becomes '$0.6\rho gz$', indicating that the overpressure is as high as 60% of the lithostatic value.

A similar calculation can be carried out for the horizontal extension regime with the overpressure (δP) formulated as

$$\delta P = \frac{2}{3}(\chi - 2)\rho gz\frac{(1-\lambda)\sin(\varphi)}{1+\sin(\varphi)}, \quad 0 \leq \chi \leq 1. \quad (15)$$

Similarly substituting $\chi = 0.5$, $\lambda = 0$ and $\varphi = 30°$, the overpressure (δP) equals to '$-1/3\rho gz$', indicating the 'underpressure' condition. In case of a hydrostatic pore fluid pressure ($\lambda = 0.4$), the overpressure (δP) is '$-1/5\rho gz$'.

Tectonic overpressure in ductile regime

As discussed in Petrini & Podladchikov (2000), rock strength in the ductile regime is a function of many potential variables including temperature, strain rate and grain size (Tsenn & Carter, 1987). Consequently, because of the chosen approach that directly links the lithospheric stresses to rock strength, the pressure is expected to be strongly sensitive to these parameters. Stüwe & Sandiford (1994) and Burov & Yamato (2008) noted that for a power-law creep rheology, the overpressure (δP) at a certain depth can be expressed as:

$$\delta P = 0.5\left(\frac{\varepsilon}{A_D}\right)^{1/n}\exp\left(\frac{E}{nRT}\right), \quad (16)$$

where A_D, n and E are material constants (as in Tables 1 & 2), R is gas constant, T is the absolute temperature and ε is the strain rate. In this case, the tectonic overpressure is coupled with depth only

Table 1. Abbreviations and units.

Symbol	Meaning	Unit
A_D	Material constant (viscous rheology)	$MPa^{-n}\ s^{-1}$
C	Cohesion (plastic rheology)	MPa
C_p	Isobaric heat capacity	$J\ kg^{-1}\ K^{-1}$
E	Activation energy	$kJ\ mol^{-1}$
F	Viscous coefficient	Dimensionless
g	Gravitational acceleration	$m\ s^{-2}$
H_a, H_r, H_S	Heat production (adiabatic, radioactive, viscous)	$W\ m^{-3}$
k	Thermal conductivity	$W\ m^{-1}\ K^{-1}$
n	Stress exponent	Dimensionless
P	Dynamic pressure	Pa
P_F	Pore fluid pressure	Pa
P_L	Lithostatic pressure	Pa
q_x, q_z	Horizontal and vertical heat fluxes	$W\ m^{-2}$
Q_L	Latent heat of melting	$kJ\ kg^{-1}$
S	Maximum shear stress	Pa
t	Time	s
T	Temperature	K
$T_{liquidus}$	Liquidus temperature of the crust	K
$T_{solidus}$	Solidus temperature of the crust	K
v_x, v_z	Horizontal and vertical components of velocity	$m\ s^{-1}$
V	Activation volume	$J\ MPa^{-1}\ mol^{-1}$
x, z	Horizontal and vertical coordinates	m
α	Thermal expansion coefficient	K^{-1}
β	Compressibility coefficient	Pa^{-1}
δP	Tectonic overpressure	Pa
$\delta P\%$	Tectonic overpressure percentage: $\delta P\% = \delta P/P_L$	Dimensionless
ε_{ij}	Components of the strain rate tensor	s^{-1}
ε_{II}	Second invariant of the strain rate tensor	s^{-2}
η	Viscosity	Pa s
λ	Pore fluid pressure coefficient: $\lambda = P_F/P_L$	Dimensionless
ρ	Density	$kg\ m^{-3}$
σ_1, σ_2, σ_3	Principal stresses	Pa
σ_{1eff}, σ_{2eff}, σ_{3eff}	Effective principal stresses	Pa
σ_{ij}	Components of the stress tensor	Pa
σ_{yield}	Yield stress	Pa
τ	Shear stress	Pa
φ	Internal frictional angle	Dimensionless
χ	Multiplier	Dimensionless

Table 2. Viscous flow laws used in numerical experiments.

ID symbol	Flow laws	E (kJ mol^{-1})	V (J MPa^{-1} mol^{-1})	n	A_D (MPa^{-n} s^{-1})	η_0[a] (Pa s)
A*	Wet quartzite	154	0	2.3	3.2×10^{-4}	1.97×10^{17}
B*	Quartzite	156	0	2.4	6.7×10^{-6}	3.75×10^{19}
C*	Plagioclase An_{75}	238	0	3.2	3.3×10^{-4}	4.80×10^{22}
D*	Mafic granulite	445	0	4.2	1.4×10^{4}	1.13×10^{21}
E*	Dry olivine	532	8	3.5	2.5×10^{4}	3.98×10^{16}
F*	Wet olivine	470	8	4.0	2.0×10^{3}	5.01×10^{20}
G*[b]	Molten felsic	0	0	1.0	2.0×10^{-9}	5×10^{14}
H*[b]	Molten mafic	0	0	1.0	1.0×10^{-7}	1×10^{13}

Source: Turcotte & Schubert (1982), Bittner & Schmeling (1995), Ranalli (1995).
[a]η_0 is the reference viscosity, which is calculated: $\eta_0 = (1/A_D) \times 10^{(6n)}$. Other parameters are illustrated in Table 1.
[b]The molten felsic (G*) are used for partial molten sediment and upper crust; the molten mafic (H*) are used for partial molten lower crust in the numerical experiments.

through the temperature field. Therefore, for a normal geothermal gradient and depth independent ε, the overpressure values decrease with depth.

Numerically testing the values of ductile overpressure with the rheological parameters of 'plagioclase An_{75}' ($A_D = 3.3 \times 10^{-4}\ MPa^{-n}\ s^{-1}$, $n = 3.2$, $E = 238\,000\ J\ mol^{-1}$, Table 2) and $R = 8.314472\ J\ K^{-1}\ mol^{-1}$, $\varepsilon = 10^{-14}\ s^{-1}$, $T = 723.15$ K (450 °C), $\delta P = 60.8$ MPa is obtained. For this temperature, and presuming that the depth $z = 35$ km, the average density $\rho = 2800\ kg\ m^{-3}$ and gravity acceleration $g = 10\ m\ s^{-2}$, the lithostatic pressure $P_L = \rho g z = 980$ MPa. The relative overpressure ($\delta P\% = \delta P/P_L$) is 6.2%.

NUMERICAL MODEL DESIGN

Numerical setup and boundary conditions

Large scale models (4000×670 km, Fig. 2) are designed for the study of dynamic processes during continental subduction/collision involving subduction of the lithospheric mantle (e.g. Pysklywec *et al.*, 2000; Burg & Gerya, 2005). A non-uniform rectangular grid with a resolution varying from 2 to 30 km is used. It provides the highest resolution (2×2 km) in the upper central, 400 km wide and 100 km deep 'orogenic' area of the model. Continuous changes in the grid spacing are prescribed on 25 nodes with ~12% grid step increment between adjacent nodes. The lithological structure of the model is represented by a dense grid of ~7 million of active Lagrangian markers used for advecting various material properties and temperature (Burg & Gerya, 2005; Gerya *et al.*, 2008).

The velocity boundary conditions are free slip at all boundaries except the lower one, which is permeable (Fig. 2). Infinity-like external free slip conditions along the lower boundary imply free slip condition to be satisfied below the base of the model at 1650 km depth (external lower boundary, outside the model frame; Burg & Gerya, 2005; Gerya *et al.*, 2008). As for the usual free slip condition, external-free slip allows global conservation of mass in the computational domain and is implemented by using the following limitation for velocity components at the lower boundary: $\partial v_x/\partial z = 0$, $\partial v_z/\partial z = -v_z/\Delta z_{external}$, where $\Delta z_{external}$ is the vertical distance from the lower boundary to the external boundary where free slip ($\partial v_x/\partial z = 0$, $v_z = 0$) is satisfied. The subducting plate is pushed leftward by prescribing a constant convergence rate (v_x) in a small internal domain that remains fixed with respect to the Eulerian coordinate (Fig. 2).

Material and thermal configuration

The initial material field (4000×670 km) is set up by a 35-km thick continental crust (17.5 km for upper crust and 17.5 km for lower crust) overlying the lithospheric mantle (115 km) and athenospheric mantle (520 km). The initiation of the subduction/collision area is imposed by a 5- to 20-km thick and 160-km deep weak zone, (Fig. 2) with a wet olivine rheology within the mantle that everywhere else has a dry olivine rheology (Table 2; Ranalli, 1995). The weak zone is prescribed to initiate continental subduction, assuming that continental subduction follows an oceanic subduction channel along which a large amount of water released from the slab formed a weak zone in the mantle (e.g.

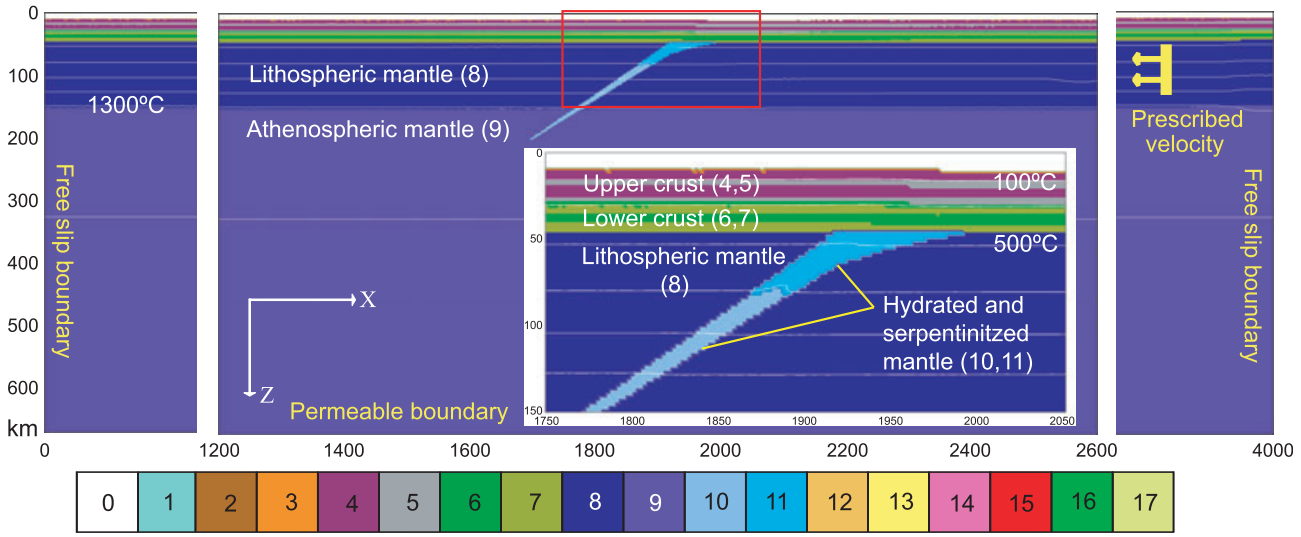

Fig. 2. Initial model configuration and boundary conditions. Enlargement (1400 × 670 km) of the numerical box (4000 × 670 km). Inset is zoomed domain corresponding to the red rectangle. Boundary conditions are indicated in yellow. White lines are isotherms measured in °C. Numbers shown in the brackets represent the rock types referring to the colourgrid (same in all the following experiment results), with: 0 – air; 1 – water; 2, 3 – sediment; 4, 5 – upper continental crust; 6, 7 – lower continental crust; 8 – lithospheric mantle; 9 – athenospheric mantle; 10, 11 – hydrated and serpentinized mantle; 12, 13 – partially molten sediment (2, 3); 14, 15 – partially molten upper continental crust (4, 5); 16, 17 – partially molten lower continental crust (6, 7). The medium-scale layering usually shares the same physical properties (e.g. 2 and 3, 4 and 5, 6 and 7, 8 and 9, and the corresponding partially molten and/or hydrated categories), with different colours used only for visualizing slab deformation and structural development. Detailed properties of different rock types are shown in Tables 2–4.

Table 3. Material properties used in numerical experiments.

Material	State	ρ_0[a] (kg m^{-3})	C_p[a] (J kg^{-1} K^{-1})	k[a] (W m^{-1} K^{-1})	$T_{solidus}$[a] (K)	$T_{liquidus}$[a] (K)	Q_L[a] (kJ kg^{-1})	H_r[a] (μW m^{-3})
Sediment and Upper Crust	Solid (2,3)[b] (4,5)[b] Molten (12,13)[b] (14,15)[b]	2800 2500	1000 1500	$[0.64 + 807/(T_K + 77)]$ exp(0.00004P_{MPa})	889 + 17 900/(P + 54) + 20 200/(P + 54)^2 at P < 1200 MPa 831 + 0.06P at P > 1200 MPa	1262 + 0.09P	300	1.75
Lower Crust	Solid (6,7)[b] Molten (16,17)	3000 2900	1000 1500	$[1.18 + 474/(T_K + 77)]$ exp(0.00004P_{MPa})	973 − 70 400/(P + 354) + 778 × 10^5/(P + 354)^2 at P < 1600 MPa 935 + 0.0035P + 0.0000062P^2 at P > 1600 MPa	1423 + 0.105P	380	0.25
Lithospheric-Athenospheric Mantle	Dry (8,9)[b] Hydrated (10,11)[b]	3300 3300	1000 1000	$[0.73 + 1293/(T_K + 77]$ exp(0.00004P_{MPa})	–	–	–	0.022
References[c]	–	1,2	–	3	4	4	1,2	1

Thermal expansion coefficient: $\alpha = 3 \times 10^{-5}$ K^{-1} and compressibility coefficient: $\beta = 1 \times 10^{-5}$ MPa^{-1} for all rock types.
[a]Meanings of symbols are illustrated in Table 1.
[b]Numbers of materials are corresponding to Fig. 2.
[c]1 = (Turcotte & Schubert, 1982); 2 = (Bittner & Schmeling, 1995); 3 = (Clauser & Huenges, 1995); 4 = (Schmidt & Poli, 1998).

Gerya *et al.*, 2002; Gerya & Stöckhert, 2006). The inclination angle of this zone increases downwards from 10° to 45°, thus simulating the curvature of the subduction plane (inset, Fig. 2). Numerical tests have shown that the initial shape of the weak zone results in efficient decoupling between the two converging plates and favours subduction of the incoming mantle lithosphere under the collisional orogen (Burg & Gerya, 2005). The material properties of all layers (Fig. 2) are listed in Tables 2–4.

The initial thermal structure of the lithosphere (white lines in Fig. 2) is laterally uniform and corresponds to a usual continental geotherm (e.g. Turcotte & Schubert, 2002): 0 °C at the surface and 1350 °C at 150 km depth. The initial temperature gradient in the asthenospheric mantle is 0.5 °C km^{-1}. The thermal boundary conditions have a fixed value (0 °C) for the upper boundary and zero horizontal heat flux across the vertical boundaries. For the lower thermal boundary, an infinity-like external constant

Table 4. Parameters of numerical experiments.

Experiments	Plastic rheology – $\sin(\varphi_{eff})$[a]			Viscous rheology – flow laws[b]					
	Crust	Dry mantle	Hydrated mantle	Sediment	Upper crust	Lower crust	Dry mantle	Hydrated mantle	Convergence rate (cm year^{-1})
MA[c]	0.12	0.48	0.06	A*	B*	C*	E*	F*	3.0
MB	0.06	-//-	-//-	-//-	-//-	-//-	-//-	-//-	-//-
MC	0.24	-//-	-//-	-//-	-//-	-//-	-//-	-//-	-//-
MD	-//-	0.24	-//-	-//-	-//-	-//-	-//-	-//-	-//-
ME	-//-	0.12	-//-	-//-	-//-	-//-	-//-	-//-	-//-
MF	-//-	-//-	-//-	-//-	-//-	-//-	E*(strong)[d]	-//-	-//-
MG	-//-	-//-	-//-	-//-	-//-	-//-	-//-	-//-	1.5
MH	-//-	-//-	-//-	-//-	-//-	-//-	-//-	-//-	5.0
MI	-//-	-//-	-//-	-//-	A*(weak)	-//-	-//-	-//-	-//-
MJ	-//-	-//-	-//-	-//-	C*(strong)	-//-	-//-	-//-	-//-
MK	-//-	-//-	-//-	-//-	-//-	B*(weak)	-//-	-//-	-//-
ML	-//-	-//-	-//-	-//-	-//-	D*(strong)	-//-	-//-	-//-

-//-, values same as the reference parameters.
[a]The plastic cohesion is zero in all the experiments. φ_{eff} is the effective internal frictional angle used for plastic rheology.
[b]The viscous rheological properties of different flow laws are shown in Table 2 with identifiers of 'A*–H*'.
[c]The reference model with reference parameters. Other parameters are shown in Table 3.
[d]The 'Strong' dry olivine flow law is implemented by decreasing the A_D value by a factor of 10^4 relative to normal dry olivine.

temperature condition is imposed, which allows both temperatures and vertical heat fluxes to vary along the permeable box lower boundary, implying constant temperature condition to be satisfied below the bottom of the model at 1650 km depth. This condition is implemented by using the limitation $\partial T/\partial z = (T_{external} - T)/\Delta z_{external}$, where $T_{external} = 2045$ °C is the temperature at the external boundary and $\Delta z_{external}$ is the vertical distance from the lower boundary to the external boundary (Burg & Gerya, 2005; Gerya *et al.*, 2008).

Viscoplastic rheological implementation

A viscoplastic rheology is assigned for the model in which the rheological behaviour depends on the minimum differential stress attained between the ductile and brittle fields.

Ductile viscosity dependent on strain rate, pressure and temperature is defined in terms of deformation invariants as:

$$\eta_{creep} = (\varepsilon_{II})^{(1-n)/2n} F (A_D)^{-1/n} \exp\left(\frac{E + PV}{nRT}\right), \quad (17)$$

where $\varepsilon_{II} = 0.5\varepsilon_{ij}\varepsilon_{ij}$ is the second invariant of the strain rate tensor and A_D, E, V and n are experimentally determined flow law parameters (Tables 1 & 2). F is a dimensionless coefficient depending on the type of experiments on which the flow law is based. For example: $F = 2^{(1-n)/n}/3^{(1+n)/2n}$ for triaxial compression and $F = 2^{(1-2n)/n}$ for simple shear.

The ductile rheology is combined with a brittle/plastic rheology to yield an effective viscoplastic rheology. For this purpose, the Mohr–Coulomb yield criterion (e.g. Ranalli, 1995) is implemented as follows:

$$\sigma_{yield} = C + P_L \sin(\varphi_{eff}), \quad (18)$$

$$\sin(\varphi_{eff}) = \sin(\varphi)(1 - \lambda),$$

$$\eta_{creep} \leq \left(\frac{\sigma_{yield}}{(4\varepsilon_{II})^{1/2}}\right),$$

where σ_{yield} is the yield stress, ε_{II} is the second invariant of the strain rate tensor, P_L is the lithostatic depth dependent pressure, C is the cohesion, φ and φ_{eff} are the (effective) internal friction angles (Brace & Kohlstedt, 1980), and λ is the pore fluid coefficient that controls the brittle strength of fluid-containing porous or fractured media.

High tectonic overpressures on the order of several hundreds of MPa are conceivable for highly constrained flows and for strong rocks, especially those strong enough to fail in a brittle manner (Mancktelow, 2008). Therefore, numerical experiments were undertaken with variable rheological properties for the crustal and mantle materials. The influences of plastic/brittle rheology are implemented by changing the sine of effective internal friction angle 'sin(φ_{eff})', which combines the effects of 'internal friction' and 'pore fluid pressure' as in eqn 18. The viscous/ductile rheologies are implemented with various flow laws by changing the experimental parameters (A_D, E, V and n in eqn 17) for the crustal and mantle layers. Detailed material properties and description of conducted numerical experiments are given in Tables 2–4.

Governing equations and numerical implementation

The momentum, continuity and heat conservation equations for a 2D creeping flow including thermal and chemical buoyant forces are solved:

1 Two-dimensional stokes equations:

$$\frac{\partial \sigma_{xx}}{\partial x} + \frac{\partial \sigma_{xz}}{\partial z} = \frac{\partial P}{\partial x}, \quad (19)$$

$$\frac{\partial \sigma_{zx}}{\partial x} + \frac{\partial \sigma_{zz}}{\partial z} = \frac{\partial P}{\partial z} - g\rho(C, M, P, T),$$

where the density ρ depends on composition (C), melt fraction (M), temperature (T) and pressure (P); g is the acceleration due to gravity.

2 Conservation of mass is approximated by the incompressible continuity equation:

$$\frac{\partial v_x}{\partial x}+\frac{\partial v_z}{\partial z}=0. \quad (20)$$

3 Heat conservation equations:

$$\rho C_p\left(\frac{DT}{Dt}\right)=-\frac{\partial q_x}{\partial x}-\frac{\partial q_z}{\partial z}+H_r+H_a+H_S+H_L \quad (21)$$

$$q_x=-k(T,P,C)\frac{\partial T}{\partial x},\quad q_z=-k(T,P,C)\frac{\partial T}{\partial z},$$

$$H_a=T\alpha\frac{dP}{dt},\quad H_S=\sigma_{xx}\varepsilon_{xx}+\sigma_{zz}\varepsilon_{zz}+2\sigma_{xz}\varepsilon_{xz},$$

where D/Dt is the substantive time derivative; x and z denote the horizontal and vertical directions respectively; the deviatoric stress tensor is defined by σ_{xx}, σ_{xz}, σ_{zz}, whereas the strain rate tensor is defined by ε_{xx}, ε_{xz}, ε_{zz}; T is the temperature, P the pressure and C the composition; q_x and q_z are heat flux components; ρ is the density, $k(T, P, C)$ is the thermal conductivity as a function of temperature, pressure and composition, C_p is the isobaric heat capacity; H_r, H_a, H_S and H_L are radioactive, adiabatic, shear and latent heat production respectively (see Table 1 for details of these parameters).

To solve the above equations, the I2VIS code (Gerya & Yuen, 2003) based on finite-differences with a marker-in-cell technique was employed, which allows for non-diffusive numerical simulation of multiphase flow in a rectangular fully staggered Eulerian grid.

RESULTS FROM NUMERICAL EXPERIMENTS

Reference model

In the reference model ('MA', Table 4), standard viscous rheological properties are used, such as 'wet quartzite' for sedimentary rocks, 'quartzite' for the upper crust, 'plagioclase An_{75}' for the lower crust and 'dry/wet olivine' for the dry/hydrated mantle (Ranalli, 1995). The plastic strength is expressed by $\sin(\varphi_{eff}) = 0.12$ for all crustal materials (sediment, upper crust and lower crust), and $\sin(\varphi_{eff}) = 0.48$ and $\sin(\varphi_{eff}) = 0.06$ for the dry and hydrated mantle materials respectively (Table 4). It is a typical assumption that the crust has lower brittle/plastic strength than the mantle because of crustal fluids. This model assumption is not disputed to provide conservative estimates of tectonic overpressure in the crustal rocks. The prescribed convergence rate is 3.0 cm year^{-1}. Detailed parameters are shown in Tables 2–4.

From the initial stage, the continental lithosphere subducts under the external push, which is prescribed on the right side of the model (Figs 2 & 3a,b). During plate convergence, the crustal rocks (especially parts of the upper crust and sedimentary rocks) continuously detach from the slab and form a ~50 km wide, wedge-like channel with forced material circulation (Fig. 3c,d). The *P–T* paths of crustal rocks show significant pressure deviation from lithostatic values (~0.3 GPa, cf. dashed and solid lines in Fig. 3a′–e′). These *P–T* paths classify rocks into three different groups of pressure history: (i) UHP-rocks subjected to significant overpressure (≥0.3 GPa) during intermediate stages of subduction (50–70 km depth, P = 1.5–2.5 GPa) enter an underpressure region at UHP depths (≥100 km, $P \geq 3$ GPa), and finally reach a region where dynamic and lithostatic pressures are equal (red, pink and green *P–T* paths, Fig. 3); (ii) HP-rocks subjected to significant overpressure (≥0.3 GPa) at peak *P–T* conditions reached at intermediate depths (50–70 km depth, P = 1.5–2.5 GPa) in the bottom corner of the wedge-like confined subduction channel (light blue, blue and yellow *P–T* paths, Fig. 3); (iii) Rocks not subjected to pressure deviation from lithostatic (black *P–T* paths, Fig. 3) remain at shallower depths (≤40 km depth, $P \leq 1$ GPa).

The evolution of tectonic overpressure magnitude in the subduction zone shows that regions of significant overpressure and underpressure are mainly located in the uppermost part of the lithospheric mantle, i.e. within a rheologically strong layer (Fig. 4). In these regions, the relatively cold mantle rocks mainly deform in brittle/plastic regime (Byerlee's law). Under lithostatic condition, the brittle/plastic strength of 1 GPa is reached at ~50 km depth (P = 1.6 GPa). However, the same strength can be reached at shallower depths (20 to 50 km) in overpressured regions [$P \leq \rho gz/(1-\sin(\varphi_{eff})$, where φ_{eff} is an effective internal friction angle, $\sin(\varphi_{eff}) = 0.6$ for dry rocks according to Byerlee's law]. Yet, such overpressured mantle rocks are rarely (or not at all in our models) exhumed to the surface, and therefore should not be seen in natural HP–UHP complexes.

Another important region of overpressure (≥0.3 GPa) is the bottom corner of the 'wedge-like' subduction channel formed at the early stages of subduction, when the external push is the main driving mechanism (Fig. 4a,a′,b,b′). This 'wedge-like' channel gradually changes to a 'planar' channel (Fig. 4-c,c′,d,d′,e,e′) when the slab pull of the subducted cold mantle lithosphere starts contributing to the force balance at the plate interface. Simultaneously, the significant overpressure (> 0.3 GPa and up to 20% of the lithostatic pressure) built in the bottom corner of the wedge-like channel (Fig. 5b) gradually decreases to several tens of MPa. In the planar subduction channel, overpressure is < 100 MPa (Fig. 5a, normally several tens of MPa) and usually < 5% of the lithostatic pressure (Fig. 5b).

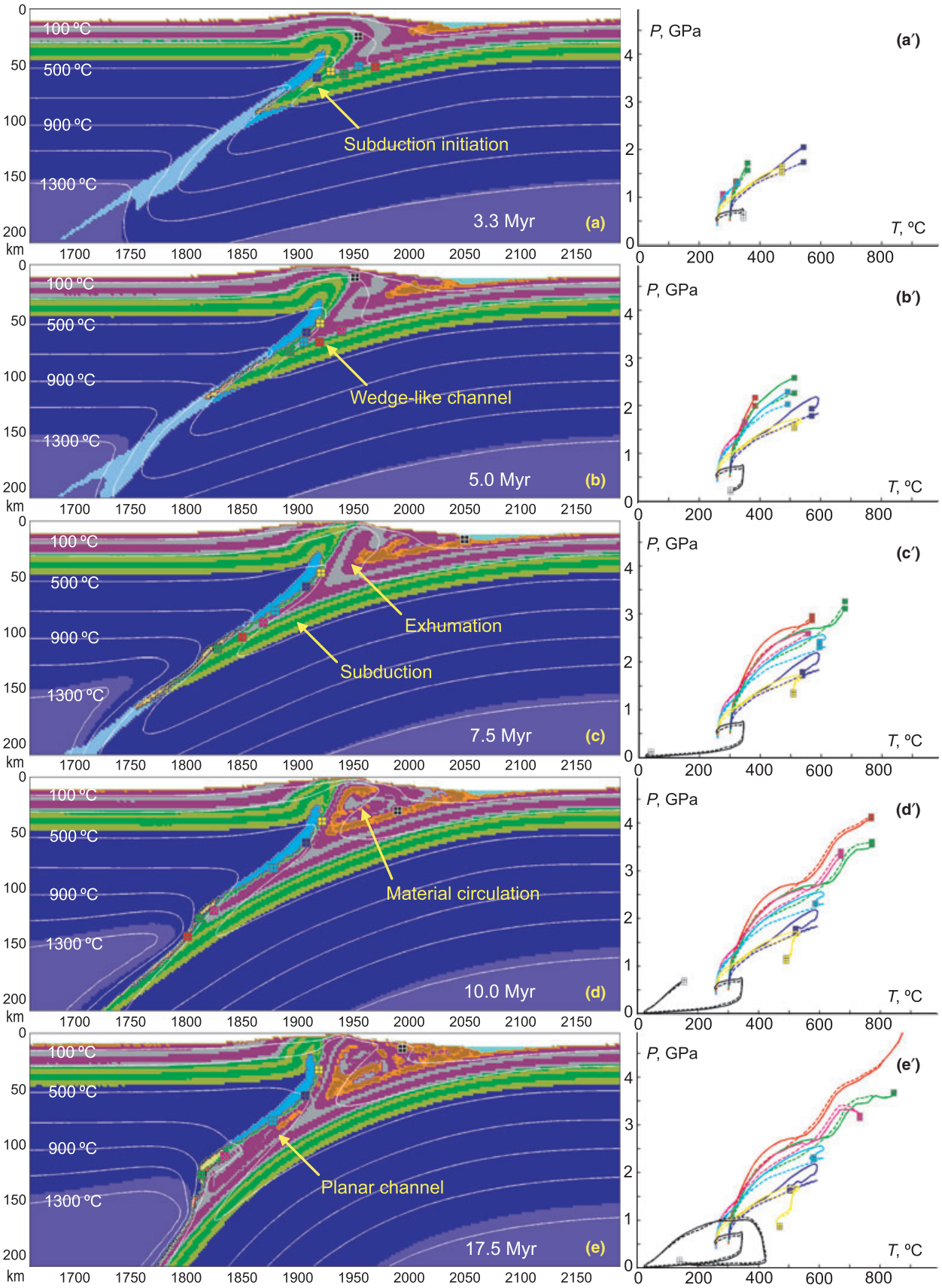

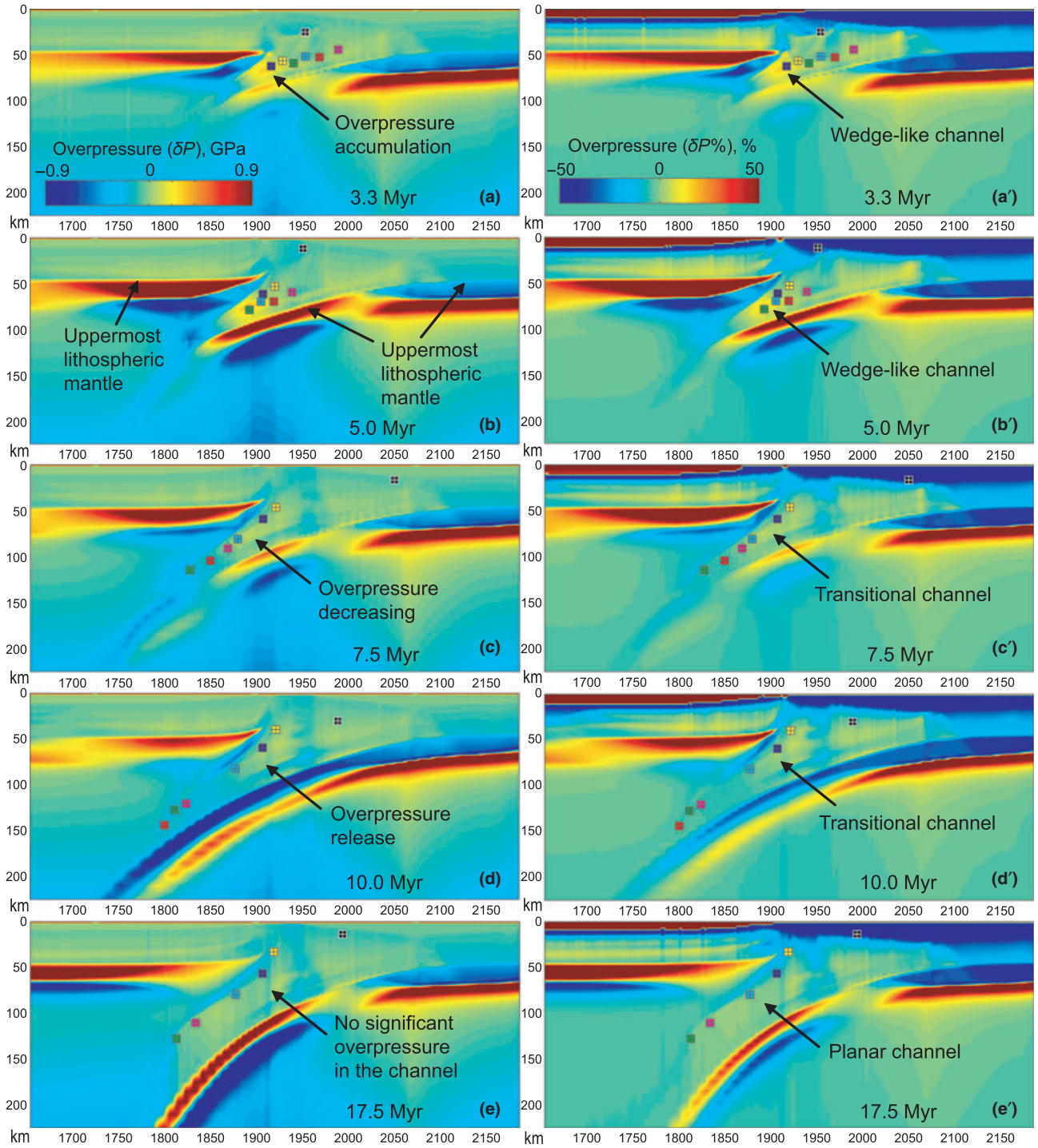

Fig. 4. The tectonic overpressure evolution of the reference model (Fig. 3). [a–e] Absolute overpressure in GPa; [a′–e′] relative overpressure (ratio between tectonic overpressure and lithostatic pressure) in per cent. The time (Myr) of shortening and tracing markers are the same as in Fig. 3.

Fig. 3. Evolution of the reference model ('MA' in Table 4) within enlarged 530 × 210 km domain of the original 4000 × 670 km model. Colours of rock types are as in Fig. 2. Time (Myr) of shortening is given in the figures. White numbered lines are isotherms in °C. Small coloured squares (with '+' in them) show positions of representative markers (rock units) for which *P–T* paths are shown (right). Colours of these squares are used for discrimination of marker points plotted in the *P–T* diagrams and do not correspond to the colours of rock types.

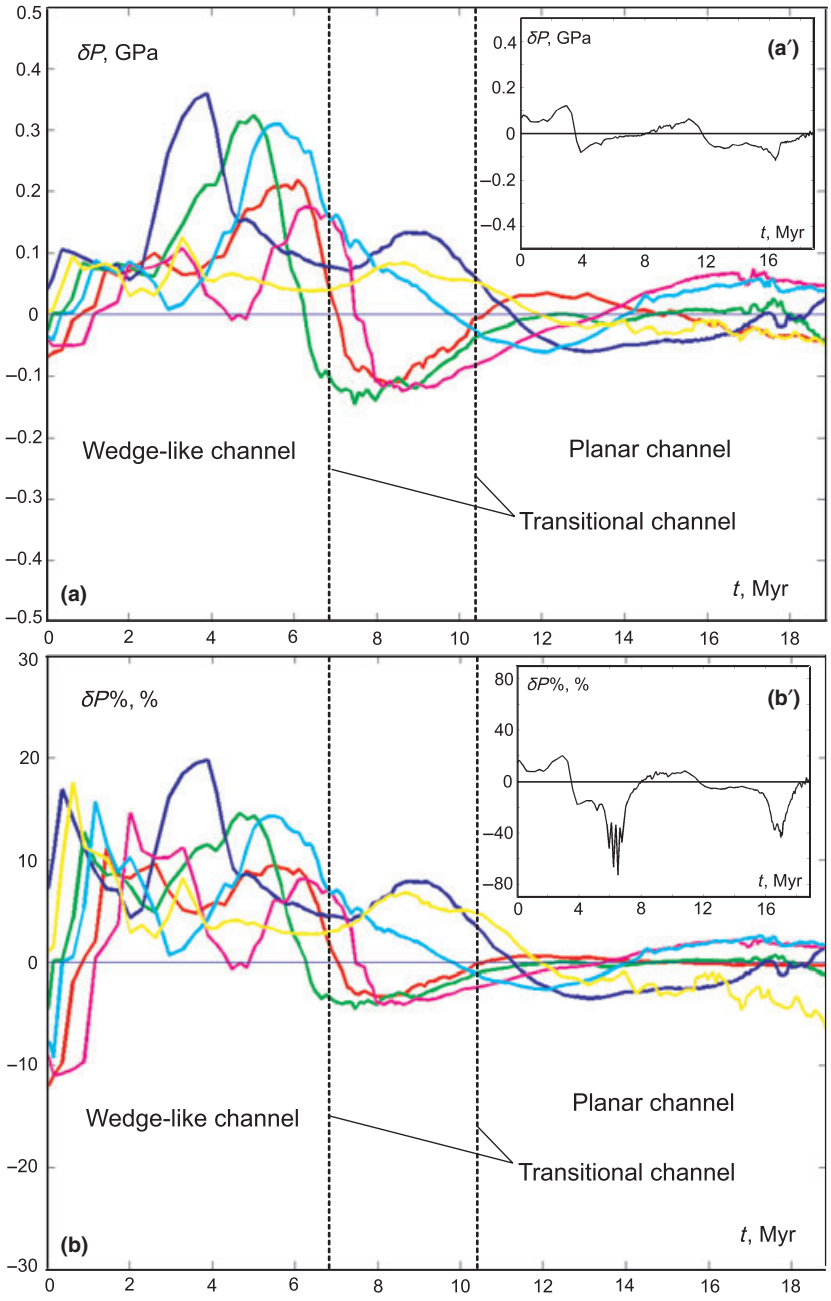

Fig. 5. The tectonic overpressure evolution through time of the tracing markers in Figs 3 & 4. [a, a′] Absolute overpressure in GPa; [b,b′] relative overpressure (ratio between tectonic overpressure and lithostatic pressure) in per cent.

Model with decreased crustal plastic strength

In the model with decreased crustal plastic strength ('MB', Table 4), subduction produces a 'wedge-like' channel in which upper/lower crustal rocks circulate (Fig. 6a–c). In contrast to the reference model, wedge-like channel geometry is stable and does not evolve into the planar channel. A pronounced 'channel neck' (e.g. Fig. 7b) spontaneously forms at the bottom of the wedge-like subduction channel. In agreement with the analytical model of Mancktelow (1995), the overpressure region (~0.3 GPa) is located above the neck whereas significant underpressure (up to 0.5 GPa) dominates bellow the channel neck along the subducting slab interface (Fig. 7a–d). The 'red marker' located in the bottom of the lower crust of the subducting slab passes through both the overpressure and underpressure zones (Fig. 7a–c, a′–c′) with sharp changes from overpressure to underpressure happening within *c.* 2 Myr (Fig. 7d,d′). The resulting *P–T* evolution is characterized by two 'bulges' characterizing positive (within *c.* 3 Myr) and then negative (within *c.* 5 Myr) deviations from lithostatic pressure along the prograde *P–T* paths

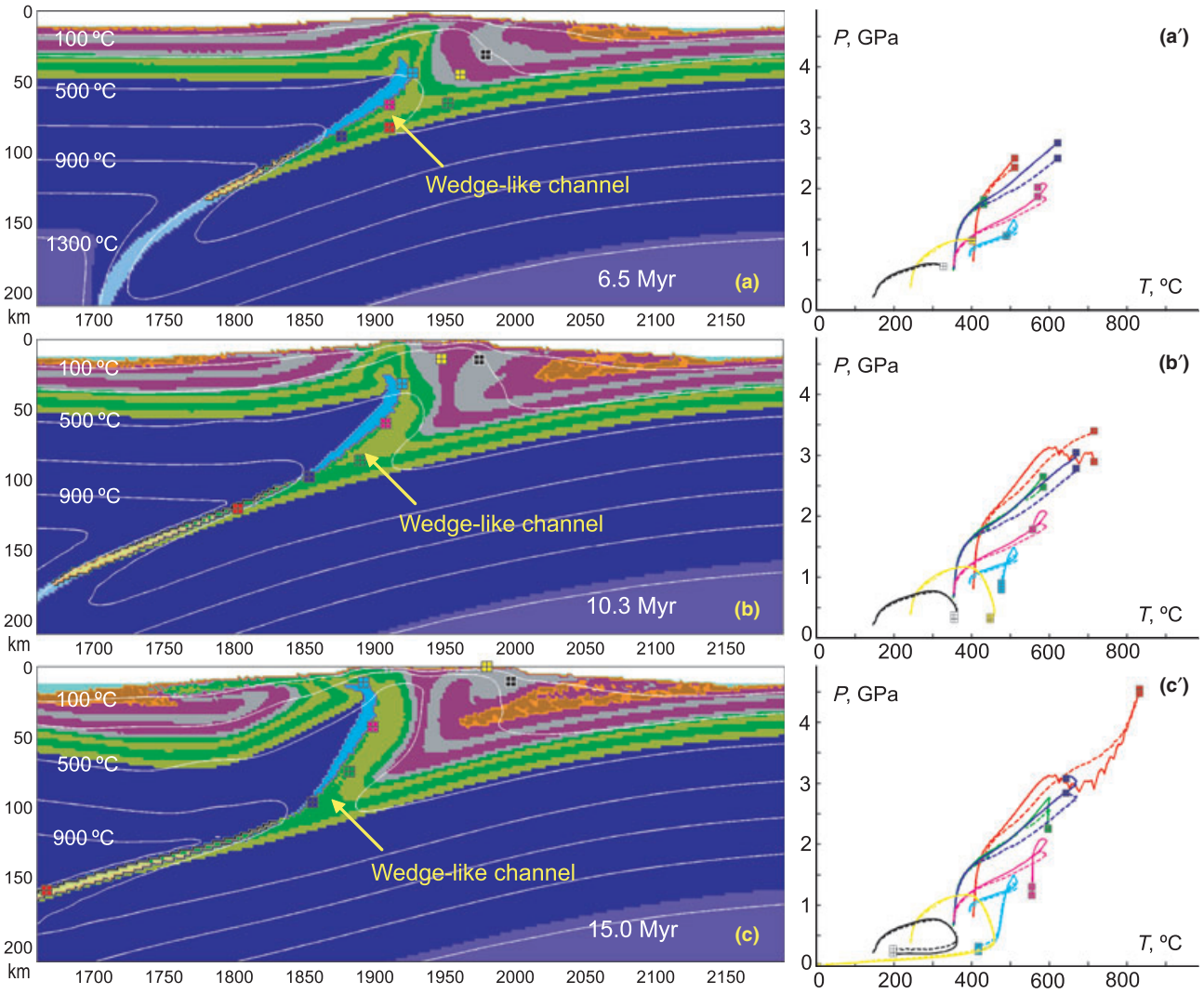

Fig. 6. Evolution of the model with decreased crustal plastic strength (model 'MB' in Table 4) within enlarged 530 × 210 km domain of the original 4000 × 670 km model. Colours of rock types are as in Fig. 2. Time (Myr) of shortening is given in the figures. White numbered lines are isotherms in °C. Small coloured squares (with '+' in them) show positions of representative markers (rock units) for which *P–T* paths are shown (right). Colours of these squares are used for discrimination of marker points plotted in the *P–T* diagrams and do not correspond to the colours of rock types.

(e.g. red curves, Figs 6c′ & 7d,d′). As in the reference model (c.f. Figs 3e′ & 6c′), *P–T* paths of the subducted crustal rocks can be classified into the same three different groups (Fig. 6a′–c′): (i) red *P–T* paths; (ii) green, pink and light blue *P–T* paths; and (iii) yellow and black *P–T* paths.

Model with increased crustal plastic strength

In the model with increased crustal plastic strength ('MC', Table 4), the subduction channel evolves from the 'wedge-like' to the 'planar' geometry, as in the reference model. Tectonic overpressure (up to 0.4 GPa and up to 40% along *P–T* paths, Fig. 8e,e′) occurs in locations that are partly different from those in the reference model: (i) the uppermost lithospheric mantle and the 'core' of upper/lower crust (① and ③ in Fig. 8a′,c′); (ii) the bottom 'corner' of the wedge-like channel (② in Fig. 8a′); (iii) the horizontal collided 'point' between the subducting and overriding slab (⑤ in Fig. 8c′); and (iv) the entrance zone of the crustal wedge (④ in Fig. 8a′,c′). Overpressures in the wedge-like channel corner (② in Fig. 8a′) and the uppermost lithospheric mantle (① in Fig. 8a′,c′) are similar to the reference model. Because of the increased plastic strength, the overriding plate crust also attains high overpressure (③ in Fig. 8a′,c′). In addition to the wedge-like channel corner (② in Fig. 8a′), two other locations of overpressure (④ and ⑤ in Fig. 8a′,c′) may affect the *P–T* paths of exhumed crustal rocks. It is worth mentioning that the overpressure accumulated at the entrance zone of the crustal wedge (④ in

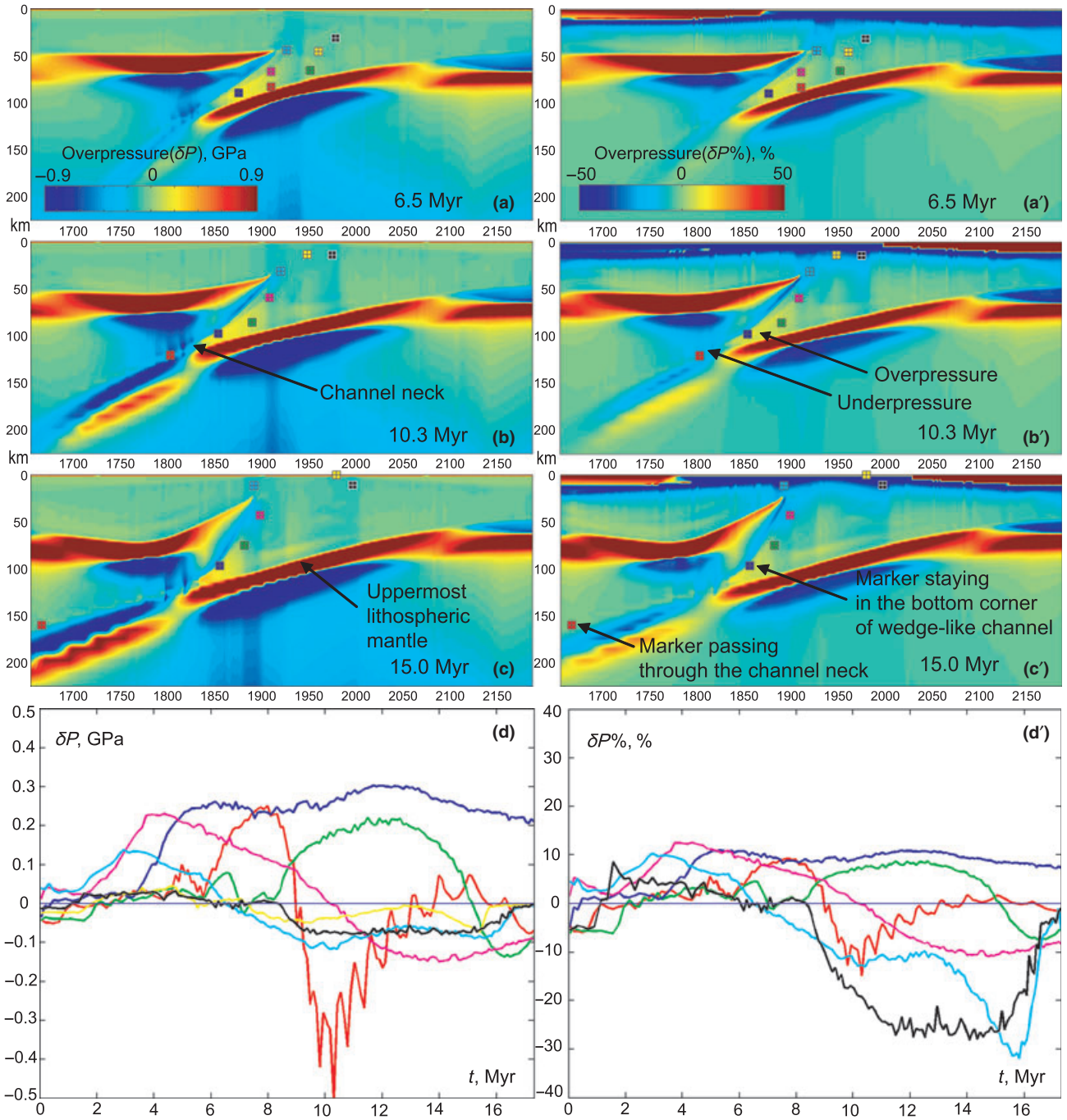

Fig. 7. The tectonic overpressure evolution of the model with decreased crustal plastic strength (Fig. 6). [a–d] Absolute overpressure in GPa; [a′–d′] relative overpressure (ratio between tectonic overpressure and lithostatic pressure) in per cent. The time (Myr) of shortening and tracing markers are the same as in Fig. 6.

Fig. 8a′,c′) is transient and released within *c.* 2 Myr due to the thrust formation within the upper part of the channel (c.f. Fig. 8c,d,c′,d′). The marker-based study of overpressure evolution through time shows the cyclicity of 'thrust faults' formation with accumulation (I, III in Fig. 8e,e′) and release (II, IV in Fig. 8e,e′) of overpressure in the subduction channel, which is described and discussed thoroughly in Li & Gerya (2009).

Influence of the mantle (confining wall) strength

Models with relatively weak mantle plastic strength ('MD', Table 4; Fig. 9) are similar to the reference

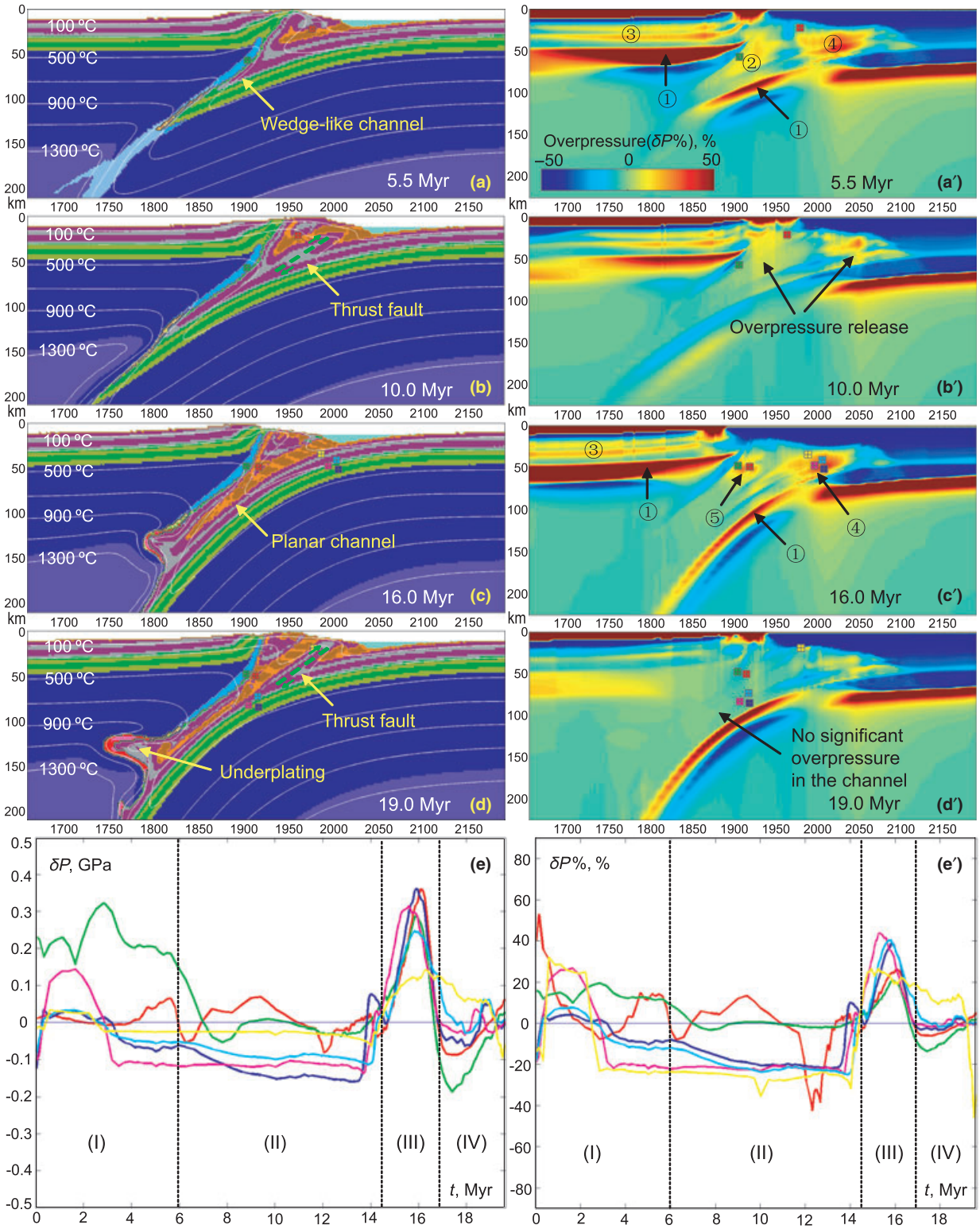

Fig. 8. Material [a–d] and relative overpressure (ratio between tectonic overpressure and lithostatic pressure) [a′–d′] evolutions of the model with increased crustal plastic strength (model 'MC' in Table 4) within enlarged 530 × 210 km domain of the original 4000 × 670 km model. Colours of rock types are as in Fig. 2. Time (Myr) of shortening is given in the figures. White numbered lines are isotherms in °C. Small coloured squares (with '+' in them) show positions of representative markers (rock units) for which the tectonic overpressure is traced [e,e′], which indicate the cyclic accumulation (I and III) and release (II and IV) of the tectonic overpressure. Colours of these squares are used for discrimination of marker points plotted in the *P–T* diagrams and do not correspond to the colours of rock types. The numbers (①–⑤) are shown as the possible locations of tectonic overpressure.

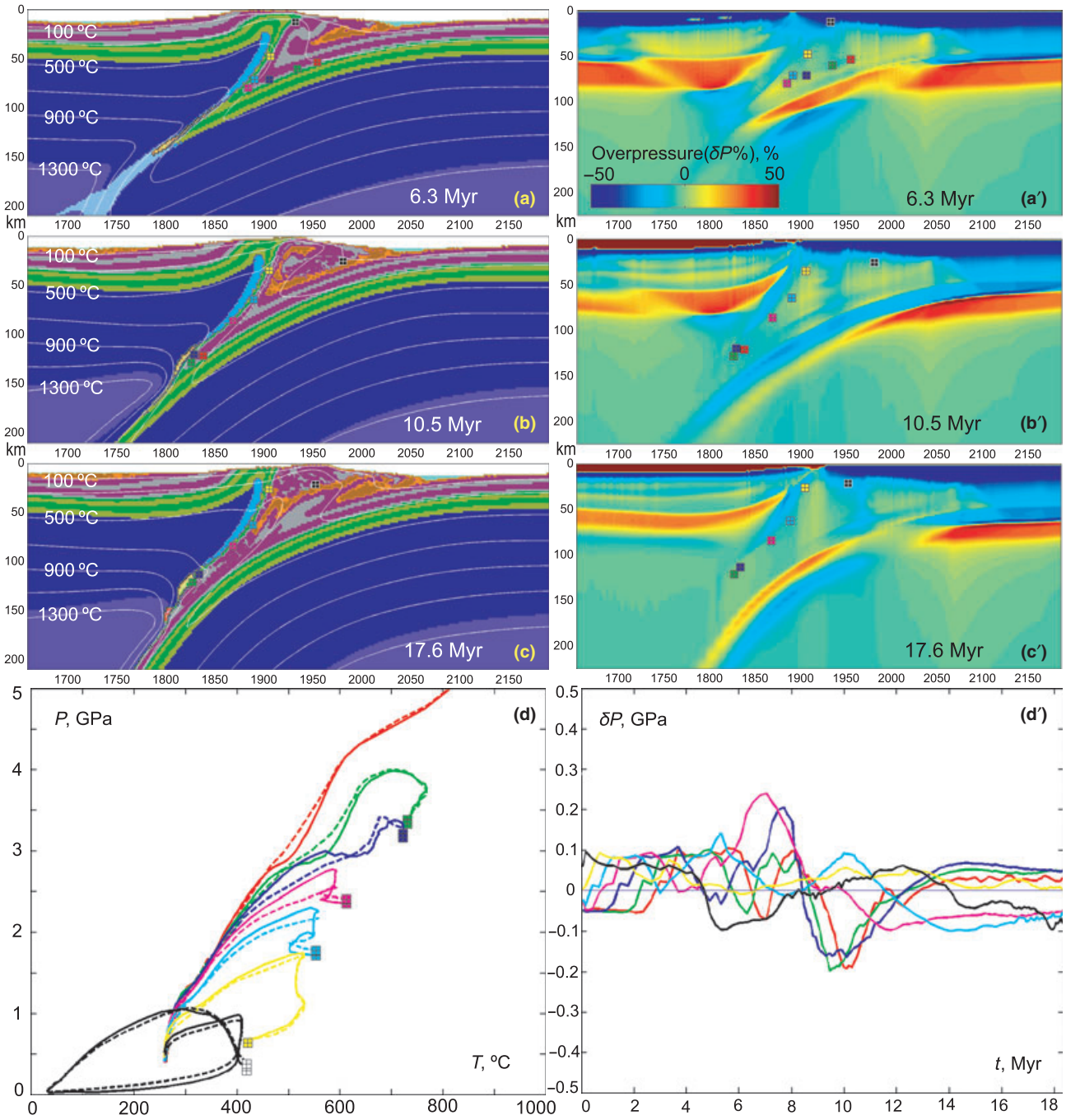

Fig. 9. Material [a–c] and relative overpressure (ratio between tectonic overpressure and lithostatic pressure) [a′–c′] evolutions of the model with weak mantle plastic strength (model 'MD' in Table 4) within enlarged 530 × 210 km domain of the original 4000 × 670 km model. Colours of rock types are as in Fig. 2. Time (Myr) of shortening is given in the figures. White numbered lines are isotherms in °C. Small coloured squares (with '+' in them) show positions of representative markers (rock units) for which the *P*–*T* paths [d] and absolute tectonic overpressure [d′] are traced. Colours of these squares are used for the discrimination of marker points plotted in the *P*–*T* diagrams and do not correspond to the colours of rock types.

model (Figs 3 & 4) with the 'wedge-like' subduction channel evolving to nearly 'planar' geometry. The peak tectonic overpressure of ~0.25 GPa, which is somewhat lower than that in the reference model (Fig. 5a), is obtained in the wedge-like channel (Fig. 9d′). A possible explanation is that the decreased strength of the mantle results in more deformation of the overriding plate (e.g. more mantle upbending in Fig. 9c compared to Fig. 3e), which decreases overpressure in the less-confined subduction channel. The model with

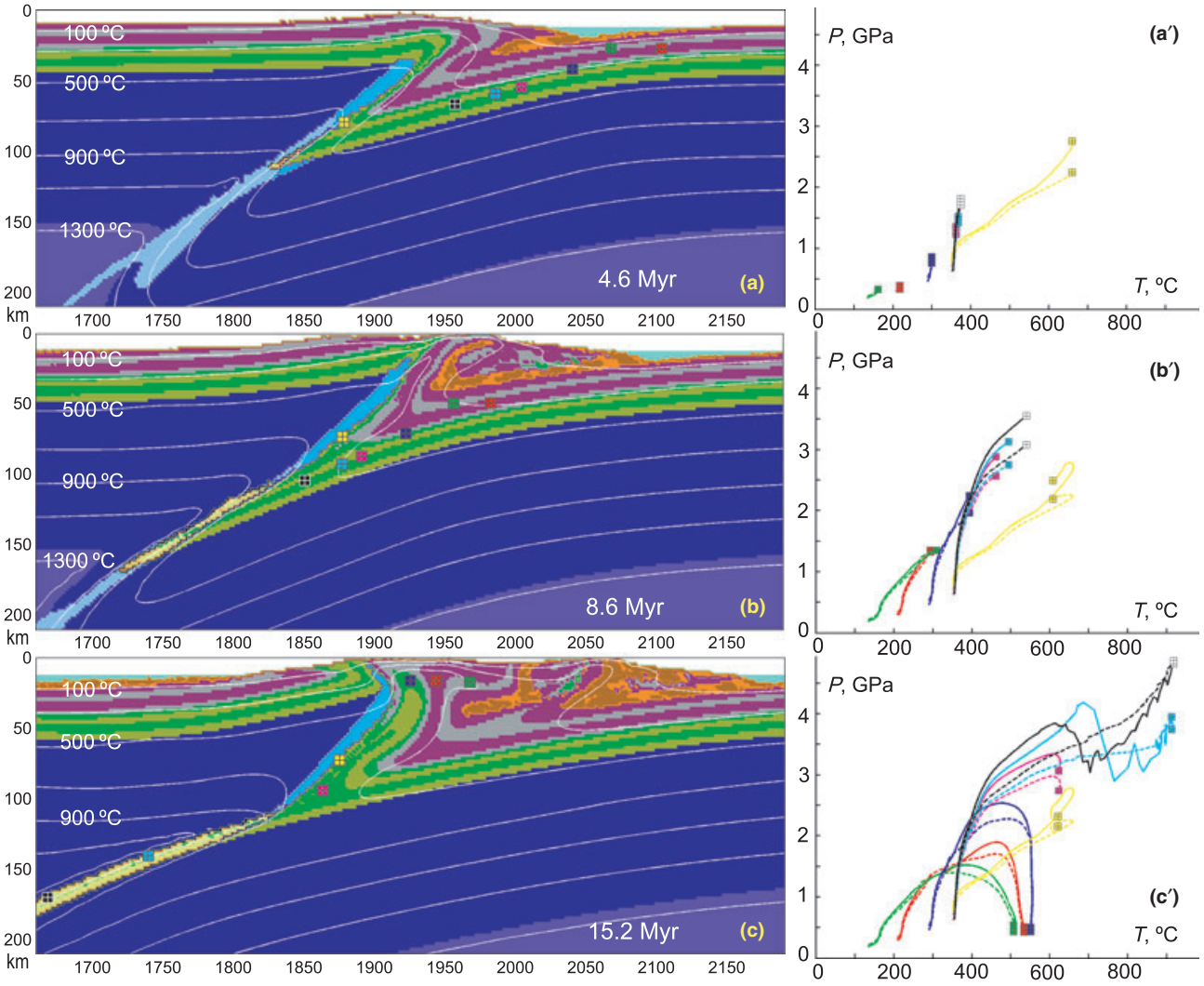

Fig. 10. Evolution of the model with higher mantle strength (model 'MF' in Table 4) within enlarged 530 × 210 km domain of the original 4000 × 670 km model. Colours of rock types are as in Fig. 2. Time (Myr) of shortening is given in the figures. White numbered lines are isotherms in °C. Small coloured squares (with '+' in them) show positions of representative markers (rock units) for which *P–T* paths are shown (right). Colours of these squares are used for the discrimination of marker points plotted in the *P–T* diagrams and do not correspond to the colours of rock types.

mantle of even lower strength ('ME', Table 2) cannot maintain subduction and instead produces pure shear thickening and buckling (e.g. Toussaint *et al.*, 2004; Agard *et al.*, 2007).

In the model with stronger confining mantle wall ('MF', Table 4; Figs 10 & 11), the subduction channel is always wedge-like, as in the model with decreased crustal plastic strength (Figs 6 & 7). This indicates that the strength contrast between crust and mantle determines the mode of the subduction channel (wedge-like and/or planar channel) with lower contrast values favouring stable wedge-like geometry. The tectonic overpressure produced in the bottom corner of the highly confined channel with rigid non-deformable walls is much larger than in all previous models with the magnitude of >0.5 GPa and even up to 1 GPa at depths of $\sim$100 km (Fig. 11d). This indicates that the highly confined wedge-like subduction channel with strong walls produces largest tectonic overpressure (see also Mancktelow, 1995).

Influence of the convergence rate

The convergence rate is one of the crucial parameters controlling the dynamics of subduction/collision processes. In order to study its influence on tectonic overpressure, experiments were conducted with both lower ('MG', Table 4) and higher ('MH', Table 4) convergence rates than the reference model.

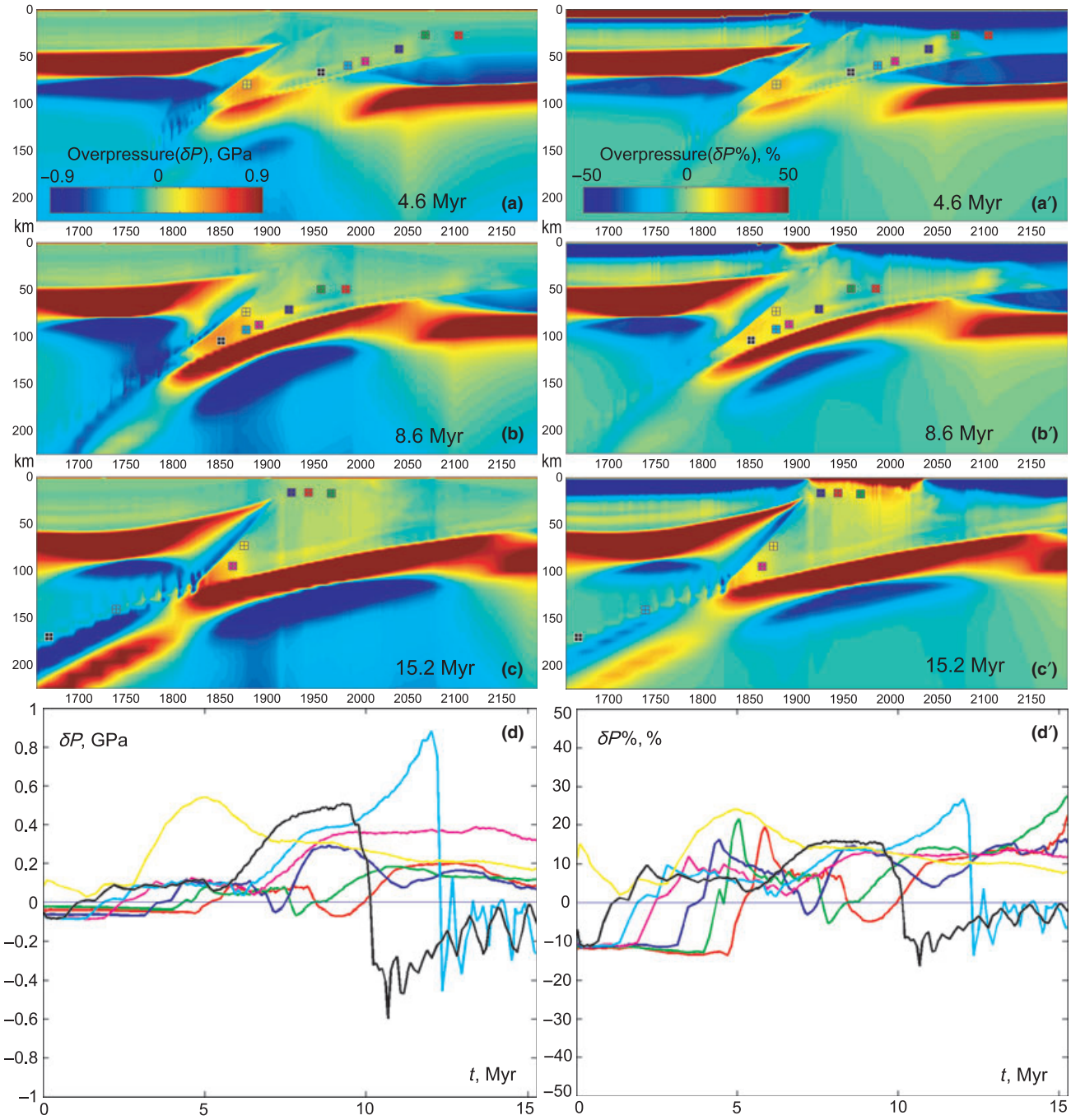

Fig. 11. The tectonic overpressure evolution of the model with higher mantle strength (Fig. 10). [a–d] Absolute overpressure in GPa; [a′–d′] relative overpressure (ratio between tectonic overpressure and lithostatic pressure) in per cent. The time (Myr) of shortening and tracing markers are the same as in Fig. 10.

The slower model (convergence rate of 1.5 cm year^{-1}) has a 'wedge-like' channel all through its evolution (Fig. 12a,a′,a″), as the model with weak crustal plastic strength (Figs 6 & 7). This means that, in the case of low convergence rate, buoyant resistance of subducting continental crust dominates the subduction drag forces and upper crustal rocks cannot subduct to UHP depths even with the relatively high plastic strength of the crust.

The faster model (convergence rate 5.0 cm year^{-1}) shows the subduction channel evolution from 'wedge-like' to 'planar' geometry (Fig. 12b,b′,b″), like the

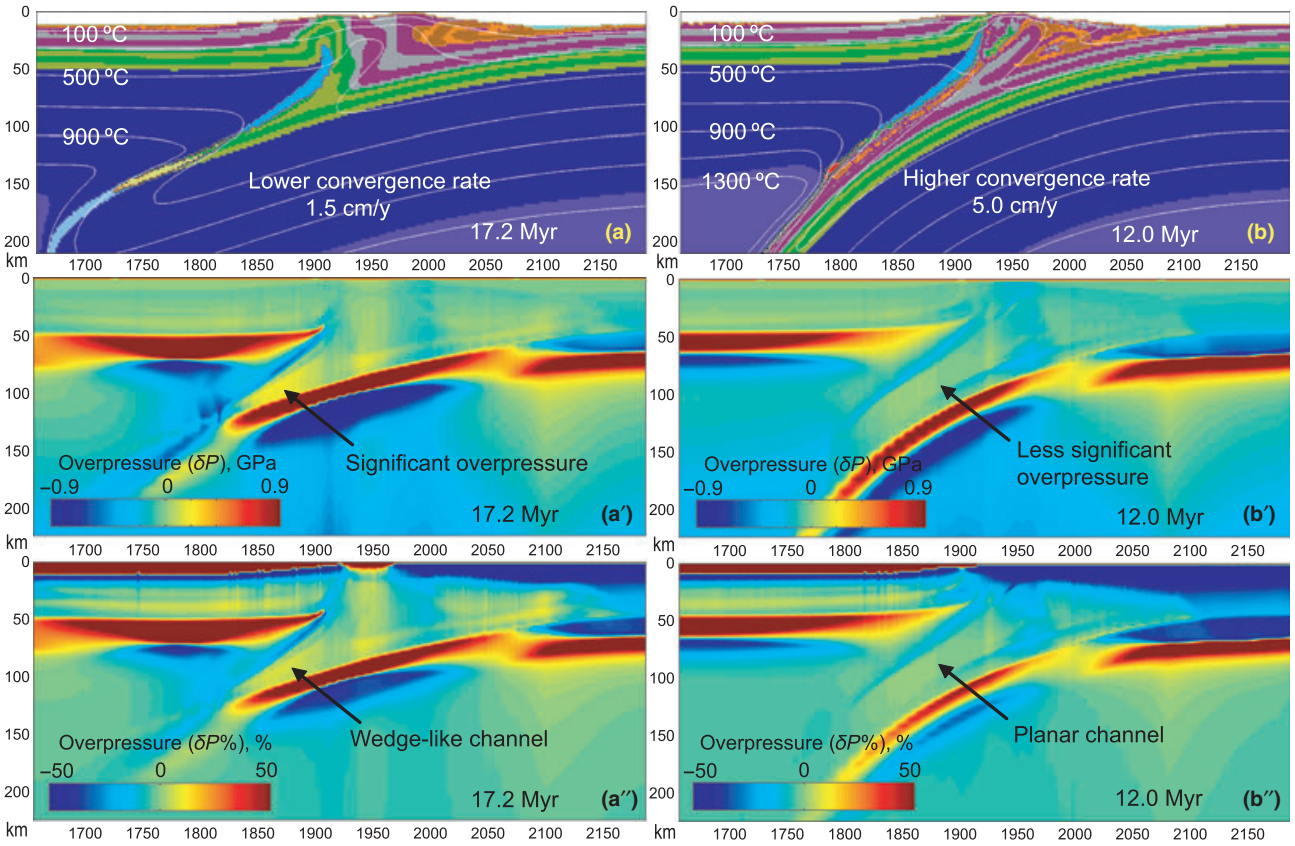

Fig. 12. The comparison models with lower [a,a′,a″] and higher [b,b′,b″] convergence rates. [a,b] Material field; [a′,b′] absolute overpressure in GPa; [a″,b″] relative overpressure (ratio between tectonic overpressure and lithostatic pressure) in per cent.

reference model (Figs 3 & 4). There is no significant overpressure in the planar channel despite the higher convergence rate.

DISCUSSION AND CONCLUSIONS

Possible influences of overpressure on natural HP–UHP rocks

In most of our numerical models (e.g. Figs 4, 7 & 8), the uppermost lithospheric mantle, that can be considered as the wall of the subduction channel, shows the largest tectonic overpressure (≥1 GPa and ≥50% of the lithostatic pressure). However, these overpressured zones rarely or never participate in the exhumation processes. Hence, they do not influence the *P–T* conditions of geologically distributed HP–UHP rocks in nature.

From the viewpoint of metamorphic record, the most important tectonic overpressure zones are identified inside the subduction channel. Two major channel types are identified: (i) wedge-like channel with notable overpressure (Figs 3b & 4b,b′) and (ii) planar channel with no significant overpressure (Figs 3e & 4e,e′). The development of either channel type depends on both the crustal and mantle rheology and on the convergence rate that, together, control the balance between the subduction drag and the buoyant resistance of subducted continental crust (e.g. Raimbourg *et al.*, 2007; Warren *et al.*, 2008). In many investigated models, a wedge-like channel forms during the early stages of collision and then evolves into a planar channel (e.g. Figs 3 & 8). The magnitude of overpressure in the wedge-like channel is controlled by the strength of the mantle: the highly confined channel with strong walls produces largest tectonic overpressure (Figs 10 & 11).

The possible consequences of tectonic overpressure on the *P–T* paths of HP–UHP rocks are summarized in Fig. 13, which shows the selected *P–T* paths from the reference model (Fig. 13a from Fig. 3e′) and the model with decreased crustal plastic strength (Fig. 13b from Fig. 6c′). As discussed earlier, the *P–T–t* evolutions are summarized by three different groups of rocks: (i) UHP-rocks with protracted history of overpressure–underpressure–lithostatic pressure (red *P–T* paths in Fig. 13); (ii) HP-rocks overpressured before exhumation (blue *P–T* paths in Fig. 13); and (iii) rocks with no pressure deviation (green *P–T* paths in Fig. 13).

The characteristic overpressure zone is located in the bottom corner of the confined wedge-like subduction

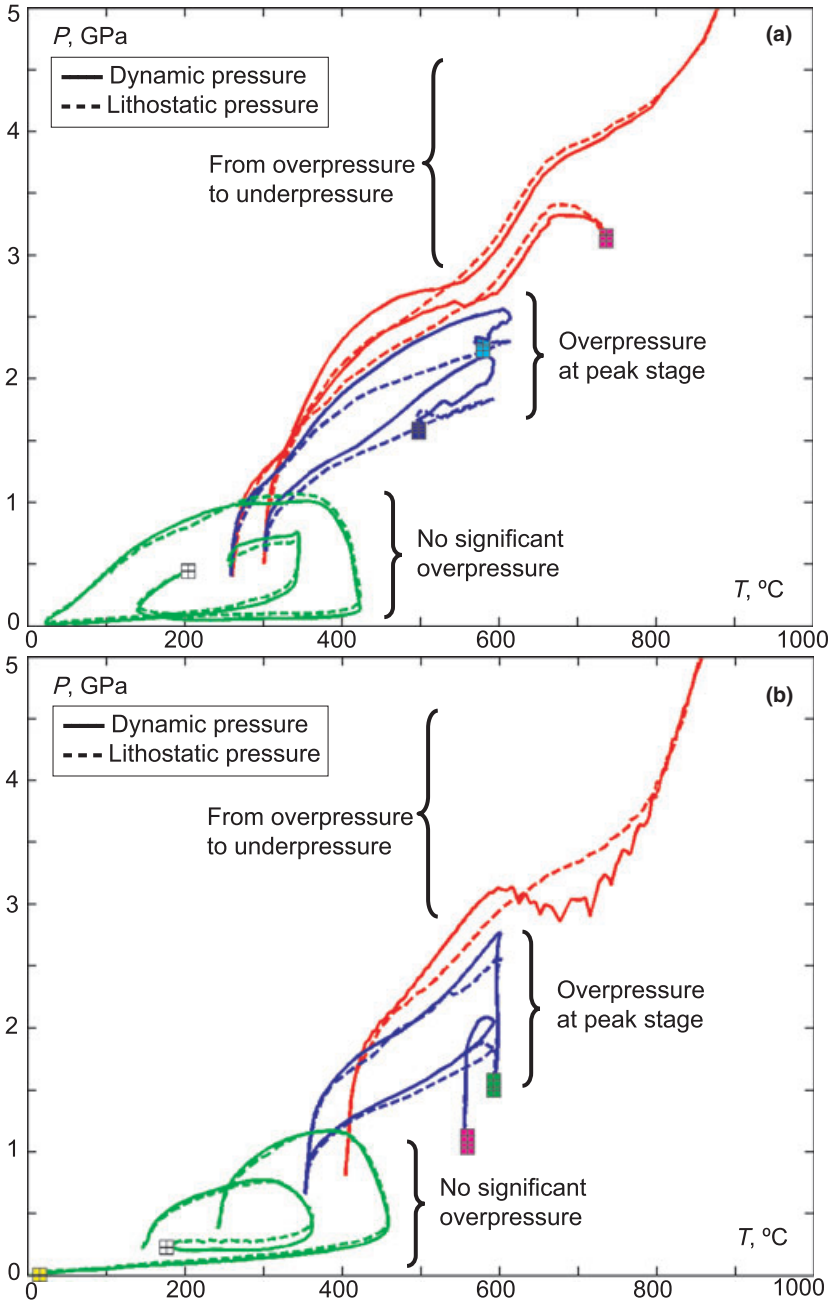

Fig. 13. [a] The selected *P–T* paths from the reference model (Fig. 3e′) and [b] the model with decreased crustal plastic strength (Fig. 6c′). Red curves: *P–T* paths of the tracing markers in UHP depth (≥3 GPa); blue curves: *P–T* paths of the tracing markers in intermediate depth (1.5–2.5 GPa); green curves: *P–T* paths of the tracing markers in shallower depth (≤1 GPa). Corresponding markers are the same as in Figs 3 & 6 respectively.

channel (e.g. Figs 4a,b,a′,b′ & 7). This zone may produce HP–UHP rocks that are exhumed back to the surface and, therefore, the following answers to the three questions formulated in introduction can be given:

1 The greatest magnitude of overpressure at HP depths of ~50 km (blue markers, Figs 3 & 4) is >0.3 GPa, which is ~20% of the lithostatic pressure (Fig. 5a,b). It indicates that a 50-km depth derived from the lithostatic principle applied to geobarometry actually is ~40 km, whereas the greatest overpressure at UHP depths of ~100 km (blue markers, Figs 6 & 7) is ~0.3 GPa and ~10% of the lithostatic pressure (Fig. 7d,d′). It means that a 100 km from lithostatic principle actually is ~90 km.

2 The overpressured rocks may participate in the exhumation processes forming geological distributed HP–UHP complexes (e.g. blue, green and pink markers in Fig. 7).

3 Rocks most strongly overpressured undergo highest pressures during the prograde *P–T* evolution for a sufficient time (a few million years) close to peak pressure (depth) conditions (e.g. blue, green, and pink and light blue *P–T* paths in Fig. 6a′–c′).

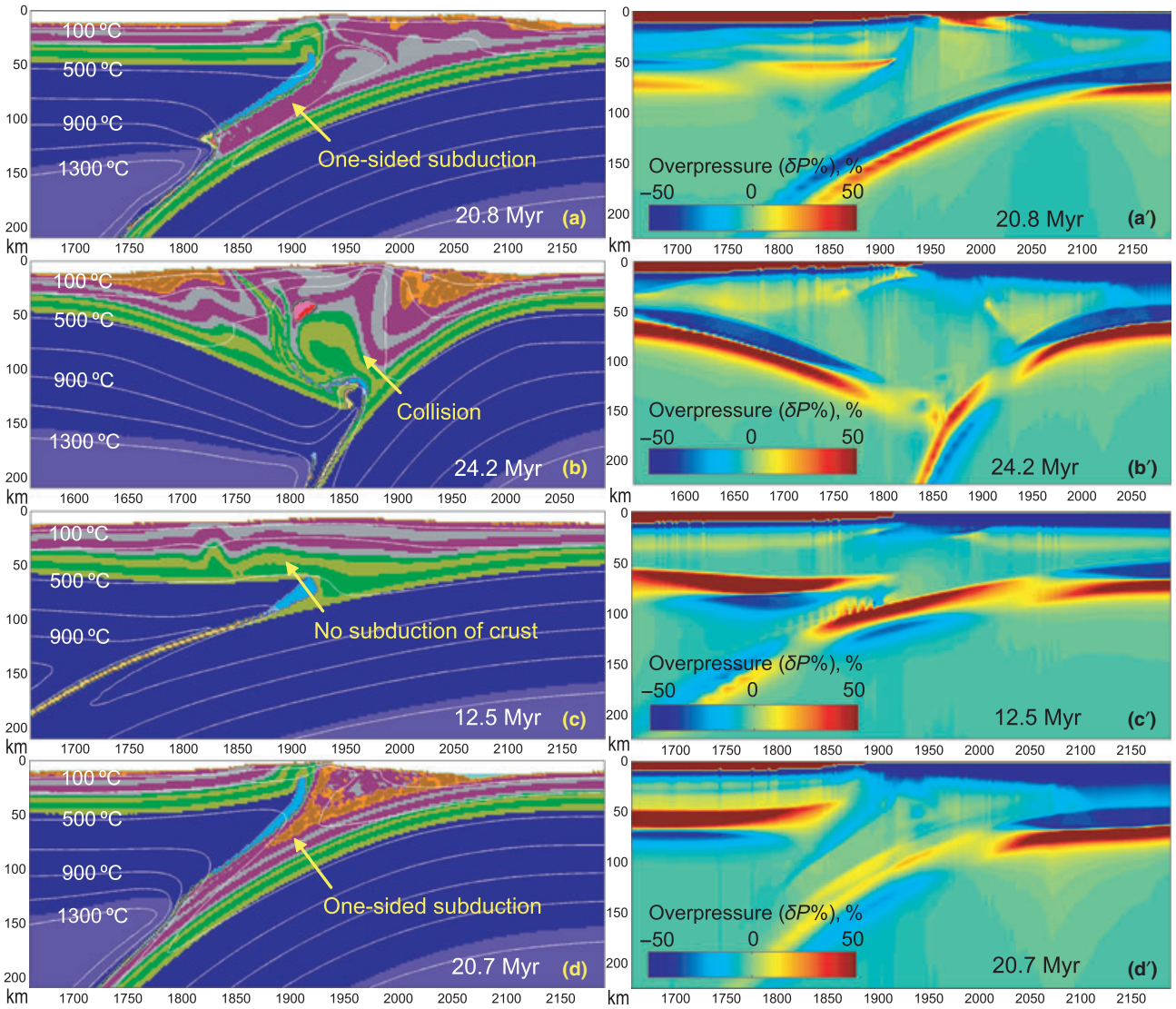

Fig. 14. The comparison models with different viscous rheologies for the upper and lower crust. [a,a′] Model with decreased strength for the upper crust (model 'MI' in Table 4); [b,b′] model with increased strength for the upper crust (model 'MJ' in Table 4); [c, c′] model with decreased strength for the lower crust (model 'MK' in Table 4); [d, d'] model with increased strength for the lower crust (model 'ML' in Table 4); [a–d] material field; [a′–d′] relative overpressure (ratio between tectonic overpressure and lithostatic pressure) field.

We emphasize that these three possibilities concern only confined wedge-like channel, which is one peculiar case (or peculiar stage) of subduction/collision zone environment. The models show that the overpressure is small (~10% lithostatic) and should not affect in a crucial way the metamorphic mineral equilibria of the exhumed UHP rocks. The challenge would be to identify the geological record to actually measure precisely such minor deviations. However, overpressure influences for HP rocks (~20% lithostatic) are notable, compared with UHP ones.

An important unresolved issue concerns the question of how the tectonic overpressure could be potentially recorded by mineral equilibria in natural rocks. Thermodynamic tools used for thermobarometry of natural rocks are mainly based on experimental data obtained under conditions of isotropic stress state (i.e. in the absence of significant deviatoric stresses) and may not be directly applicable for recording dynamic pressure in strongly stressed rocks. Indeed, not all overpressured rocks should be strongly internally stressed. For example, weak (e.g. reacting, fluid rich) rock inclusions in strong overpressured stressed lithosphere will also have strong overpressure, but the stress state will be isotropic, i.e. similar to the conditions of laboratory experiments. This isotropic stress (dynamic pressure) will be notably different from the lithostatic pressure, which will then be directly recorded by

mineral equilibria of such rock inclusions. Obviously further efforts are needed to experimentally study mineral equilibria in stressed rocks.

Tectonic overpressure in variable styles of plate convergence

The above-mentioned study of tectonic overpressure focuses on the general one-sided subduction with three-layer material configuration. However, there are many different subduction/collision and exhumation scenarios (e.g. Burov & Yamato, 2008), in which the influence of overpressure is expected to be different. Figure 14 shows several cases with different viscous rheological parameters for the crustal rocks ('MI, MJ, MK, ML', Table 4). In all of these models, tectonic overpressures are not as significant in the mature subduction channel and/or the inner collision belt, which suggests that the overpressure that can possibly affect the HP–UHP rocks is mainly related to the wedge-like confined subduction channel (e.g. Figs 6 & 7).

ACKNOWLEDGEMENTS

We acknowledge the fund from China Scholarship Council (CSC) and the support from the 973 Project of Chinese Ministry of Science and Technology (2003CB716504) to ZHL. This work was supported by ETH Research Grants TH-12/05-3, TH-0807-3; SNF Research Grants 200021-113672/1, 200021-116381/1; and the RF President Program 'Leading Scientific School of Russia' (Grant No. 1949.2008.5) to TVG. Fruitful discussions with N. Mancktelow are greatly appreciated. Thorough and critical reviews by the invited editor L. Dobrzhinetskaya and two anonymous reviewers are gratefully acknowledged.

REFERENCES

Agard, P., Jolivet, L., Vrielynck, B., Burov, E. & Monié, P., 2007. Plate acceleration: the obduction trigger? *Earth and Planetary Science letter*, **258,** 428–441.

Bittner, D. & Schmeling, H., 1995. Numerical modeling of melting processes and induced diapirism in the lower crust. *Geophysical Journal International*, **123,** 59–70.

Brace, W.F. & Kohlstedt, D.T., 1980. Limits on lithospheric stress imposed by laboratory experiments. *Journal of Geophysical Research*, **85,** 6248–6252.

Brace, W.F., Ernst, W.G. & Kallberg, R.W., 1970. An experimental study of tectonic overpressure in Franciscan rocks. *Geological Society of America Bulletin*, **81,** 1325–1338.

Burg, J.-P. & Gerya, T.V., 2005. The role of viscous heating in Barrovian metamorphism of collisional orogens: thermomechanical models and application to the Lepontine Dome in the Central Alps. *Journal of Metamorphic Geology*, **23,** 75–95.

Burov, E. & Yamato, P., 2008. Continental plate collision, *P-T-t-z* conditions and unstable vs. stable plate dynamics: insights from thermo-mechanical modelling. *Lithos*, **103,** 178–204.

Burov, E., Jolivet, L., Le Pourhiet, L. & Poliakov, A., 2001. A thermomechanical model of exhumation of high pressure (HP) and ultra-high pressure (UHP) metamorphic rocks in Alpine-type collision belts. *Tectonophysics*, **342,** 113–136.

Byerlee, J.D., 1978. Friction of rock. *Pure and Applied Geophysics*, **116,** 615–626.

Chopin, C., 1984. Coesite and pure pyrope in high-grade blueschists of the Western Alps: a first record and some consequences. *Contributions to Mineralogy and Petrology*, **86,** 107–118.

Chopin, C., 2003. Ultrahigh-pressure metamorphism: tracing continental crust into mantle. *Earth and Planetary Science letter*, **212,** 1–14.

Clauser, C. & Huenges, E., 1995. Thermal conductivity of rocks and minerals. in: *Rock physics and phase relations* (ed Ahrens, T.J.), American Geophysical Union, Reference Shelf 3, Washington D.C, pp. 105–126.

Coleman, R.G. & Lee, D.E., 1962. Metamorphic aragonite in the glaucophane schists of Cazadero, California. *American Journal of Science*, **260,** 577–595.

Dobrzhinetskaya, L., Posukhova, T., Trønnes, R., Korneliussen, A. & Sturt, B.A., 1993. A microdiamond from eclogite-gneiss area of Norway. *International Eclogite Conference, 4th, Terra Nova Abstract Supplement: Oxford, Blackwell Scientific*, **5,** 9.

Dobrzhinetskaya, L.F., Braun, T.V., Sheshkel, G.G. & Podkuiko, Y.A., 1994. Geology and structure of diamond-bearing rocks of the Kokchetav massif (Kazakhstan). *Tectonophysics*, **233,** 293–313.

Dobrzhinetskaya, L.F., Eide, E.A., Larsen, R.B. *et al.*, 1995. Microdiamond in high-grade metamorphic rocks of the Western Gneiss region, Norway. *Geology*, **23,** 597–600.

Ernst, W.G., 1971. Do mineral parageneses reflect unusually high-pressure conditions of Franciscan metamorphism?. *American Journal of Science*, **270,** 81–108.

Gerya, T.V., Stöckhert, B. & Perchuk, A.L., 2002. Exhumation of high-pressure metamorphic rocks in a subduction channel: A numerical simulation. *Tectonics*, **21,** 6, 1056.

Gerya, T.V. & Yuen, D.A., 2003. Characteristics-based marker-in-cell method with conservative finite-differences schemes for modelling geological flows with strongly variable transport properties. *Physics of Earth and Planetary Interior*, **140,** 293–318.

Gerya, T.V. & Stöckhert, B., 2006. Two-dimensional numerical modeling of tectonic and metamorphic histories at active continental margins. *International Journal of Earth Sciences*, **95,** 250–274.

Gerya, T.V., Perchuk, L.L. & Burg, J.-P., 2008. Transient hot channels: perpetrating and regurgitating ultrahigh-pressure, high-temperature crust-mantle associations in collision belts. *Lithos*, **103,** 236–256.

Green, H.W., 2005. Psychology of a changing paradigm: 40+ years of high-pressure metamorphism. *International Geology Review*, **47,** 439–456.

Li, Z. & Gerya, T.V., 2009. Polyphase formation and exhumation of HP-UHP rocks in continental subduction zone: numerical modelling and application to the Sulu UHP terrane in eastern China. *Journal of Geophysical Research*, **114,** B09406; doi: 10.1029/2008JB005935.

Liou, J.G., Tsujimori, T., Zhang, R.Y., Katayama, I. & Maruyama, S., 2004. Global UHP Metamorphism and Continental Subduction/Collision: the Himalayan Model. *International Geology Review*, **46,** 1–27.

Mancktelow, N.S., 1993. Tectonic overpressure in competent mafic layers and the development of isolated eclogites. *Journal of Metamorphic Geology*, **11,** 801–812.

Mancktelow, N.S., 1995. Nonlithostatic pressure during sediment subduction and the development and exhumation of high-pressure metamorphic rocks. *Journal of Geophysical Research*, **100,** 571–583.

Mancktelow, N.S., 2008. Tectonic pressure: theoretical concepts and modelled examples. *Lithos*, **103,** 149–177.

Okay, A.I., Xu, S. & Sengör, A.M.C., 1989. Coesite from the Dabie Shan eclogites. *European Journal of Mineralogy*, **1,** 595–598.

Petrini, K. & Podladchikov, Y., 2000. Lithospheric pressure-depth relationship in compressive regions of thickened crust. *Journal of Metamorphic Geology*, **18,** 67–77.

Pysklywec, R.N., Beaumont, C. & Fullsack, P., 2000. Modelling the behavior of the continental mantle lithosphere during plate convergence. *Geology*, **28,** 655–658.

Raimbourg, H., Jolivet, L. & Leroy, Y., 2007. Consequences of progressive eclogitization on crustal exhumation, a mechanical study. *Geophysical Journal International*, **168,** 379–401.

Ranalli, G. & Murphy, D.C., 1987. Rheological stratification of the lithosphere. *Tectonophysics*, **132,** 281–295.

Ranalli, G., 1995. *Rheology of the Earth, Deformation and Flow Processes in Geophysics and Geodynamics*, 2nd edn. Chapman & Hall, London, UK.

Renner, J., Stöckhert, B., Zerbian, A., Roller, K. & Rummel, F., 2001. An experimental study into the rheology of synthetic polycrystalline coesite aggregates. *Journal of Geophysical Research-Solid Earth*, **106,** 19411–19429.

Rosen, O.M., Zorin, Y.M. & Zayachkovsky, A.A., 1972. A find of a diamond linked with eclogites of the Precambrian Kokchetav massif. *Dokladi Akademii Nauk SSSR*, **203,** 674–676 (in Russian).

Rutland, R.W.R., 1965. Tectonic overpressures. In: *Controls of Metamorphism* (eds Pitcher, W.S. & Flinn, G.W.), pp. 119–139. Boyd, Edinburgth.

Schmidt, M.W. & Poli, S., 1998. Experimentally based water budgets for dehydrating slabs and consequences for arc magma generation. *Earth and Planetary Science Letter*, **163,** 361–379.

Smith, D.C., 1984. Coesite in clinopyroxene in the Caledonides and its implications for geodynamics. *Nature*, **310,** 641–644.

Sobolev, N.V. & Shatsky, V.S., 1990. Diamond inclusions in garnets from metamorphic rocks: a new environment for diamond formation. *Nature*, **343,** 742–745.

Stüwe, K. & Sandiford, M., 1994. Contribution of deviatoric stresses to metamorphic *P-T* paths: an example appropriate to low-*P*, high-*T* metamorphism. *Journal of Metamorphic Geology*, **12,** 445–454.

Toussaint, G., Burov, E. & Jolivet, L., 2004. Continental plate collision: unstable vs. stable slab dynamics. *Geology*, **32,** 33–36.

Tsenn, M.C. & Carter, N.L., 1987. Upper limits of power law creep of rocks. *Tectonophysics*, **136,** 1–26.

Turcotte, D.L. & Schubert, G., 1982. *Geodynamics*, 450. John Wiley, New York.

Turcotte, D.L. & Schubert, G., 2002. *Geodynamics*, 2nd edn. Cambridge University Press, Cambridge, UK.

Wang, X., Liou, J.G. & Mao, H.K., 1989. Coesite-bearing eclogite from the Dabie Mountains in central China. *Geology*, **17,** 1085–1088.

Warren, C.J., Beaumont, C. & Jamieson, R.A., 2008b. Formation and exhumation of ultra-high pressure rocks during continental collision: role of detachment in the subduction channel. *Geochemistry Geophysics Geosystems*, **9,** Q04019; doi: 10.1029/2007GC001839.

Xu, S., Okay, A.I., Ji, S. *et al.*, 1992. Diamond from the Dabie Shan metamorphic rocks and its implication for tectonic setting. *Science*, **256,** 80–82.

Received 16 March 2009; revision accepted 19 November 2009.